Dynamics and non-equilibrium structure of colloidal dumbbell-shaped particles in dense suspensions

Dissertation
zur Erlangung des akademischen Grades

doctor rerum naturalium
(Dr. rer. nat.)

im Fach Physik
Spezialisierung: Theoretische Physik

eingereicht an der
Mathematisch-Naturwissenschaftlichen Fakultät
der Humboldt-Universität zu Berlin

von

Diplom-Physiker
Nils Heptner

Präsident der Humboldt-Universität zu Berlin
Prof. Dr. Jan-Hendrik Olbertz

Dekan der Mathematisch-Naturwissenschaftlichen Fakultät
Prof. Dr. Elmar Kulke

Gutachter:

Prof. Dr. Joachim Dzubiella

Prof. Dr. Benjamin Lindner

Prof. Dr. Holger Stark

Tag der mündlichen Prüfung: 21. April 2016

Abstract

Besides being important for industrial applications, colloidal suspensions have long served as model systems, both in experiments and theory, for investigating the structure and dynamics of condensed matter. The simplest colloidal system, a suspension of hard spheres, already exhibits an elaborate phase diagram. Additional intriguing phenomena, such as the plastic crystal (PC) phase, are introduced if particles are anisotropic. PCs are characterised by crystalline centre of mass (COM) ordering while they lack long-range order in the particles' orientations. Recently, it has been demonstrated experimentally that, in contrast to hard spheres, apparently a small anisotropy is sufficient to dramatically change the viscoelastic response under external shearing fields, of which the microscopic mechanisms are not yet sufficiently understood.

In the present work, non-equilibrium Brownian dynamics (NEBD) simulations of colloidal hard dumbbells in oscillatory shear fields are developed and employed to elucidate the novel findings in close connection with comprehensive rheology and small-angle neutron scattering (SANS) experiments. Furthermore, by utilising Brownian dynamics (BD) simulations and linear response theory, the impact of anisotropy on structure and dynamics of such suspensions in equilibrium is analysed. In the linear response limit, the shear viscosity exhibits a dramatic increase at high packing fractions beyond a critical anisotropy of the particles. This indicates that, even for the small investigated anisotropies, newly occurring, collective rotational-translational couplings must be made responsible for slow time scales appearing in the PC.

Moreover, a non-equilibrium transition emerging at moderate aspect ratios is revealed by NEBD of plastic crystalline suspensions under oscillatory shear. The transition behaviour is systematically studied with respect to the particles' aspect ratio at various frequencies and strains. It is demonstrated that the continuous nature of the transition is retained for very low aspect ratios only. Above a certain aspect ratio, the transition is mediated by an intermediate disordered state. Furthermore, a partially oriented sliding layer state featuring a finite collective order in the particles' orientations is observed at high strains.

Hence, this thesis demonstrates that the NEBD simulations explain novel phenomena in rheology and scattering experiments. In the light of these experiments, it is shown that the orientational degree of freedom has a vigorous impact on the structural transition under increasing oscillatory shear.

Key words: Dumbbells, Colloids, Soft Matter, Brownian dynamics, Non-equilibrium steady states

Zusammenfassung

Neben ihrer Bedeutung in industriellen Anwendungen dienen Kolloide seit langem als Modellsysteme in Experimenten und in der Theorie, um die Struktur und Dynamik von kondensierter Materie zu untersuchen. Das einfachste kolloidale System, harte Kugeln in Suspension, zeigt bereits ein komplexes Phasendiagramm. Weitere faszinierende Phänomene, wie die „Plastic-Crystal"-Phase (PC), können bei anisotropen Teilchen beobachtet werden. PCs sind durch kristalline Ordnung der Massenzentren gekennzeichnet, während die Ausrichtung der Teilchen keine langreichweitige Ordnung aufweist. Kürzlich wurde experimentell gezeigt, dass offenbar eine kleine Anisotropie ausreicht, um die viskoelastische Antwort unter externen Scherfeldern im Vergleich zu harten Kugeln drastisch zu ändern. Die mikroskopischen Ursachen hierfür sind bisher noch nicht hinreichend verstanden.
In dieser Arbeit werden daher „non-equilibrium Brownian dynamics (NEBD)"-Simulationen von harten kolloidalen Dumbbells in oszillatorischen Scherfeldern entwickelt und eingesetzt, um diese neuen Resultate mit enger Verbindung zu umfangreichen Rheologie- und Neutronenstreuexperimenten zu erklären. Weiterhin wird die Bedeutung der Anisotropie für Struktur und Dynamik von solchen Suspensionen im Gleichgewicht mit Hilfe von „Linear-Response"-Theorie und Brownian dynamics (BD)-Simulationen analysiert.
Im linearen Limit zeigt die Scherviskosität bei hohen Packungsdichten einen dramatischen Anstieg jenseits eines kritischen Anisotropieparameters. Dies weist darauf hin, dass schon bei den kleinen Anisotropien, neuartige kollektive Rotations-Translations-Kopplungen für langsame Zeitskalen im PC verantwortlich sein müssen.
Weiterhin wird ein Nichtgleichgewichtsübergang bei moderaten Aspektverhältnissen mittels NEBD-Simulationen von dichten Suspensionen harter Dumbbells im PC unter oszillatorischer Scherung ersichtlich. Dieser Übergang wird systematisch in Hinsicht auf das Aspektverhältnis der Teilchen bei verschiedenen Frequenzen und Amplituden untersucht. Es wird gezeigt, dass der kontinuierliche Übergang nur für sehr kleine Aspektverhältnisse erhalten bleibt. Oberhalb eines bestimmten Aspektverhältnisses wird der Übergang durch einen ungeordneten Zustand vermittelt. Außerdem wird ein teilweise orientierter Sliding-Layer Zustand mit endlicher kollektiver Ordnung der Teilchenausrichtung bei hohen Scheramplituden beobachtet. Somit zeigt diese Arbeit, dass die NEBD-Simulationen neuartige Phänomene in Rheologie- und Streuexperimenten erklären. Angesichts dieser Experimente wird gezeigt, dass der Orientierungsfreiheitsgrad einen starken Einfluss auf den strukturellen Übergang bei steigenden Amplituden hat.
Schlagwörter: Dumbbells, Kolloide, Weiche Materie, Brownsche Dynamik, Stationäre Nichtgleichgewichtszustände

Contents

Publications

This thesis contains work from the following original papers published in peer-reviewed journals:

F. Chu, M. Siebenbürger, F. Polzer, C. Stolze, J. Kaiser, M. Hoffmann, N. Heptner, J. Dzubiella, M. Drechsler, Y. Lu, and M. Ballauff, "Synthesis and characterization of monodisperse thermosensitive dumbbell-shaped microgels.", Macromol. Rapid Commun. **33**, 1042–1048 (2012).

F. Chu, N. Heptner, Y. Lu, M. Siebenbürger, P. Lindner, J. Dzubiella, and M. Ballauff, "Colloidal plastic crystals in a shear field", Langmuir **31**, 5992–6000 (2015).

N. Heptner, and J. Dzubiella, "Equilibrium structure and fluctuations of suspensions of colloidal dumbbells", Mol. Phys. **113**, 2523–2530 (2015).

N. Heptner, F. Chu, Y. Lu, P. Lindner, M. Ballauff, and J. Dzubiella, "Nonequilibrium structure of colloidal dumbbells under oscillatory shear", Phys. Rev. E **92**, 052311 (2015).

Chapter 1

Introduction

Colloidal suspensions are systems of particles immersed in a solvent, also commonly referred to as *complex fluids*, in which the solute particles move significantly slower than the solvent particles. The sizes of the colloidal particles roughly range from a few nanometers up to the micrometer scale, whereas typical solvent molecules, such as water, are in the Ångström range. The observation of the undirected and seemingly erratic motion of colloidal particles has led to a strong backing of the atom hypothesis [1, 2]. It has allowed calculation of the size and number of molecules driving the *Brownian motion* [3]. Despite the undirected and irregular nature of the movements, Einstein's and Smoluchowski's predictions of a linearly growing mean square displacement has been verified by Perrin [1–3], who was, at the same time, able to calculate Avogadro's number. The huge difference in the typical time scales of motion of a solvent molecule and a colloidal particle leads to a separation of the dynamics. This fact allows one to regard the influence of the suspending medium as a very short-time correlated random process. Moreover, one typically defines the *Brownian time*, τ_B, describing the time that is needed for a particle to cover a distance of its own size. Beyond this time, the motion can be considered overdamped, which means that the motion is no longer systematically ballistic in its character.

Applications of colloidal systems While there are plenty of colloidal products in our daily lives, such as dairy products [4], cosmetics and paint, recent advances in chemical synthesis allow production of functional colloids as well as self-propelled or complexly shaped particles [5–8]. On one hand, there are practical considerations for the use of colloids in a variety of fields, such as drug delivery [9]. On the other hand, fascinating systems can be designed to address fundamental questions. Mutually attached spheres, for example, are sometimes referred to as *colloidal molecules* as

they resemble atomic molecules in their shapes and it is possible to control the bond-angles [10, 11]. A nice overview has been presented by Glotzer and Solomon, for a small excerpt see fig. 1.1. Thus, colloids may be regarded as models for atomic or molecular systems, which simplify the investigation of analogue systems due to slower time scales and larger sizes of the particles [12]. Moreover, on this fundamental level colloids enable the understanding of the mechanisms of phase transitions and arrested states [13].

The colloidal complexity is not solely defined by the particles' shapes but also by their interactions, which can be tailored to allow for interpenetration and clustering of colloidal particles [14–16]. Furthermore, functional particles can adsorb and release macromolecules or nanoparticles, change dimensions upon thermal or chemical stimuli, or catalyse reactions [17, 18]. Assemblies of colloidal particles can be used as coatings or provide porous structures after evaporation of the suspending medium or removing the colloidal particles [19]. In this respect, colloidal suspensions may be used as building blocks for material structures, and colloidal self assembly can be applied to manufacture materials such as membranes with novel functionality [20].

Also, colloidal crystals can be considered as photonic band gap materials [21–25], which may allow for selective inhibition of light from travelling in a medium.

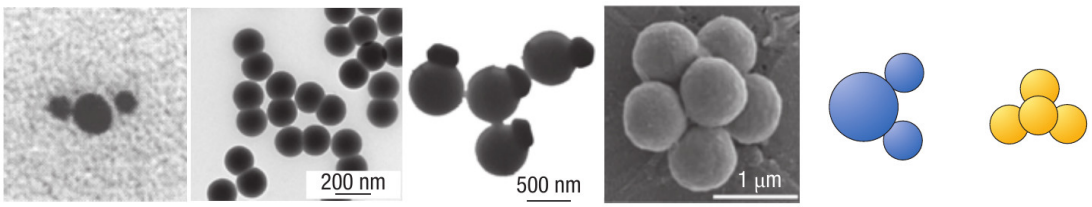

Figure 1.1: Examples of colloidal molecules made from identically or differently sized spheres. Reprinted with permission from S. C. Glotzer, and M. J. Solomon, Nat. Mater. **6**, 557–562 (2007) [8]. Copyright © 2007, Nature Publishing Group.

The hard sphere model system There are a vast number of regular and irregular shapes of colloidal particles in fundamental research, industry, nature and our everyday lives [4]. Nevertheless, extensive research has allowed for for exploration of suspensions of spherical particles with only excluded volume interaction as a model system extensively and revealed a great variety of phenomena, such as vitrification and crystallisation and complex non-equilibrium behaviour [26–29]. There is a plethora of literature on hard sphere colloids in equilibrium and non-equilibrium conditions. Due to the many intriguing open questions, there is an active community

dealing with perfectly spherical colloids [28, 30–32]. Beyond the concept of point particles, potentials with spherical symmetry lacking all structure except for infinite repulsion upon contact is the simplest model considered, see fig. 1.2 for a sketch of the phase diagram. Due to the excluded volume of such spheres with finite extent the hard sphere system exhibits an entropy-driven freezing transition [31, 33, 34]. In between, the fluid and crystal phases coexist. Above a packing fraction ϕ of ca. 58 % of the volume a kinetically arrested glassy state can be observed up to the random close packing limit at 64 % [35, 36]. At about 74 % spheres are close-packed, which relates to the densest packing problem that has captivated scientists for centuries [37]. This simple interaction potential allows analytic calculation of many important physical properties of a hard sphere system. Nevertheless, this knowledge can be applied to more sophisticated systems as well, which can have repulsive or partly attractive interactions [26, 38]. Thus, the colloidal *hard sphere* system has

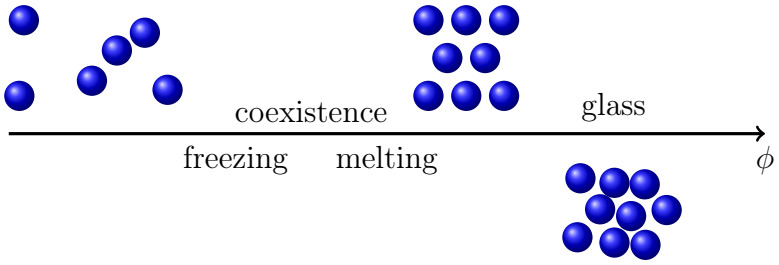

Figure 1.2: Sketch of the hard sphere phase diagram showing an entropy driven freezing transition and a kinetically arrested glass state.

been of interest in a great number of disciplines and topics. This interest is, at least in part, due to the system's simplicity and the rich physical insight the system provides [33].

Anisotropic colloids In general, colloidal particles are anisotropic in shape and interaction, which was considered in the light of mineral sheets, rod-like viruses and flexible polymer chains by Perrin Onsager in the 1930s and 1940s [39–41]. Suspensions of anisotropic particles have been studied by many researchers, e.g. spherocylinders as models for micro-organisms [42, 43].

In equilibrium the anisotropy gives rise to novel phases, such as the PC or rotator phase, nematic or liquid crystalline states [44–49]. Furthermore, the anisotropy of the suspended particles may be of great importance for dynamical quantities as well as structural formation under external fields [50, 51]. To address such fundamental questions, well-defined experimental and theoretical model systems are needed. One of the simplest realisations of mildly anisotropic colloids are

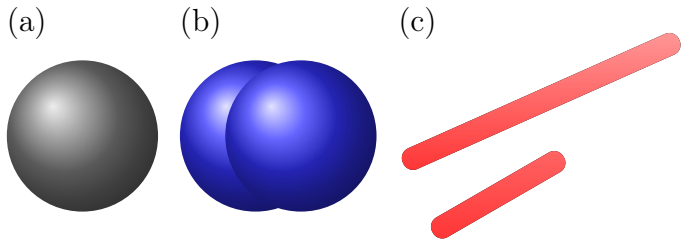

Figure 1.3: From isotropic to anisotropic model systems: spherical particles (a), mildly anisotropic dumbbells (limited aspect ratio at touching spheres) (b) and rods with arbitrary aspect ratios (c).

dumbbell-shaped particles (that is, a dimer of two fused identical colloidal spheres, cf. fig. 1.3) which can be synthesised by using different routes in well-controlled and monodisperse ways [22, 52–62]. In the search for a well-behaved experimental hard dumbbell system, a number of groups have proposed synthetic specimen [52, 53, 62–64], that differ in their interactions, their size distributions and dimensions. With respect to particle interactions, residual attractive potentials play a role when aiming at a stable hard model system, as attractive forces can also lead to irreversible aggregation [65] and introduce additional complications in the phase behaviour [66, 67]. The literature on hard spheres and related systems shows that polydisperse systems are inhibited from crystallisation [31, 68–70]. This fact is exploited when preparing samples in a disordered high density state to investigate glass formation or prevent glassy systems from crystallising [71, 72]. For comparison with computational models, monodispersity is also a desirable feature when studying crystallisation, as it is hindered in polydisperse suspensions.

Phase behaviour of hard dumbbells The phase diagram of hard-core dumbbells is theoretically known [45, 73–79]. Early Monte Carlo (MC) investigations of Vega et al. have been intensified by Marechal and Dijkstra [76, 77]. At high packing fractions, the colloids can form the so-called PC or *rotator* phase [45, 74–79] in which the translational degrees of freedom are essentially frozen at high packings as in the hard sphere system but the particles are free to rotate. Adjacent to this region, the phase diagram features re-entrant freezing and melting transitions with changing aspect ratio, i.e. the ratio of the length to the width given by the diameter of a sphere. Figure 1.4 depicts the phase diagram of the hard dumbbell system in the volume fraction ϕ and aspect ratio plane. In the context of dumbbell systems, the aspect ratio is usually expressed as the elongation $L^* = L/D$ defined by the ratio of the distance of the centres of the spheres to their diameter. At elongations

$L^* \geq 0.4$ the PC phase ceases to exist and a direct transition from the fluid to the close packed (CP) phase divided by a coexistence region is possible, while at elongations close to unity a dense aperiodic phase exists [77, 80, 81]. The ϕ-axis of

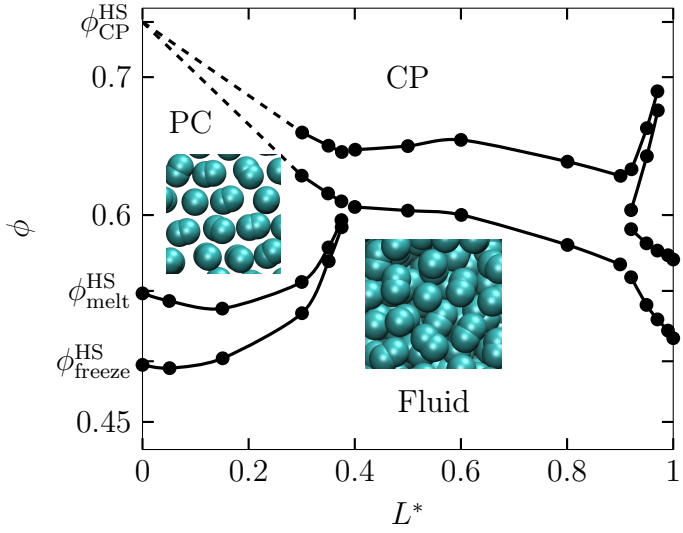

Figure 1.4: Phase diagram of the hard dumbbell system, data is taken from ref. [77]. The fluid (F), plastic crystal (PC), close packed (CP) and aperiodic phases and the respective coexistence regions are shown in the elongation (L^*) - volume fraction (ϕ) plane. The insets show snapshots of the fluid (F) phase and the 111-plane of the PC, respectively.

the dumbbell phase diagram coincides with the hard sphere phase diagram, where the system is fully crystalline above the melting density due to the lack of an orientational degree of freedom.

Colloids in external fields Fascinating phenomena are observed in colloids under the influence of external fields [82]. In processing suspensions, various kinds of external fields are applied to colloids, which may be electrical [83], magnetic, thermal, flow fields or gravity, to name some [84]. In fact, even walls or confining boundaries can be seen as a method of external control. The application of external fields can change the equilibrium of the system [85], lead to non-equilibrium steady states or drive the system into full transient non-equilibrium [86]. Under gravity, for example, the coexistence of different phases may be observed due to density gradients [87]. Very recently, Liu et al. have been able to align rods in a PC phase by switching electrical fields [50]. Forster et al. have suggested dumbbell colloids as field-switchable photonic crystals [22]. Besides the choice of external potentials, the design of the particles may be used to target self-assembly, e.g. by introducing

metal cores in otherwise dielectric particles [60]. Moreover, in an electrical field, percolation transitions of patchy particles can be induced [88]. External control of colloidal assembly can also be achieved by using patterned substrates or optical fields acting as potentials [89].

A very important class of external fields are flow fields, which can be arbitrarily complicated. This spatial or temporal complexity is strongly dependent on the boundary conditions and the driving forces causing media to flow. One of the most elementary flows is the simple shear flow, where the velocity is unidirectional and depends linearly on the distance from the walls. This *Couette flow* is the laminar solution for two plates of which one is moving and the other is fixed at a certain distance with no-slip boundary conditions [90]. Shear flows are very common in processing and transport of material as they are inevitably present due to typical boundary conditions on the flowing medium. In order to analyse the response of a medium to shear, one typically chooses simple shear with an oscillatory or steady time dependence. In the context of colloidal flow, shear can lead to a multitude of phenomena: Shear fields may be used to induce crystallisation in colloidal hard sphere glasses [91, 92] or drive gelation in dilute suspensions of charge-stabilised particles [93]. It may be desirable to prevent crystallisation or glass formation in a process, as solidification can hamper the transport of material.

Non-equilibrium structure and shear response Intriguingly, shear flows can be employed to induce order in otherwise disordered colloids [94, 95]. They can form string-like structures, free slipping layers, registered moving layers or crystal-like order [96, 97], while strong shearing also can be used to melt ordered equilibrium structures [98]. Under shear conditions, various non-equilibrium states have been identified in spherical colloids, which have been well characterised using a combination of scattering methods [99, 100], optical techniques [101, 102], simulations [102] and theoretical models [103]. The structure of driven suspensions of hard spheres has been extensively investigated by means of light scattering [100, 104] and direct observation by microscopes [101, 102], where various shear protocols have been employed, such as steady shear, sinusoidal oscillatory shear and fixed rate oscillatory shear. Similar order-disorder transitions of colloids under shear have been reported for clusters of soft spheres [16] and highly charged spheres [105, 106]. Dense suspensions of spherical charge-stabilised particles with long-range order at rest show a polycrystalline state at low shear rates and long-range sliding layer order at higher shear rates, where the transition is accompanied by a drop in the shear viscosity [107, 108]. Additionally, particle tracking methods have shed light on the

modes of motion in these stationary structures [109, 110].

In the early work by Ackerson and Pusey, light scattering and shear conditions have been combined, without measuring the rheological response [100]. Further insight has been gained from direct optical observation of induced order in sheared suspensions [101]. Most recently, Besseling et al. have combined confocal microscopy and BD simulations to explore the non-equilibrium behaviour of colloidal hard spheres under oscillatory shear [102]. In their study, a greater range of frequencies and strain amplitudes has been explored, yielding a complex non-equilibrium state diagram for sheared suspensions of hard spheres [102]. Here, for small strains a fcc twin sketched in fig. 1.5 is found to be stable corroborating with the classical results [100].

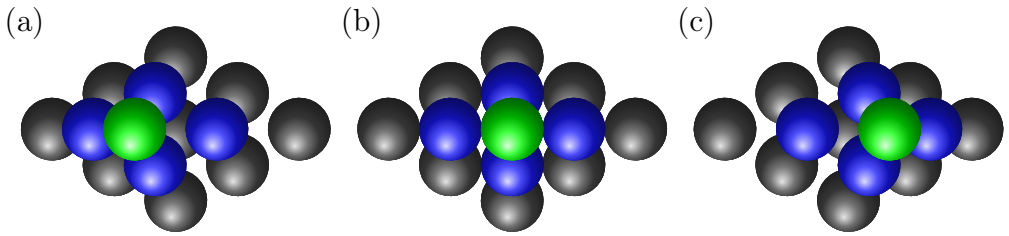

Figure 1.5: Sketch of the shear twinned fcc crystal of hard spheres. Hexagonal close packed (hcp) layers are (a),(c) registered at the oscillatory shear extrema and (b) bridge-stacked in between.

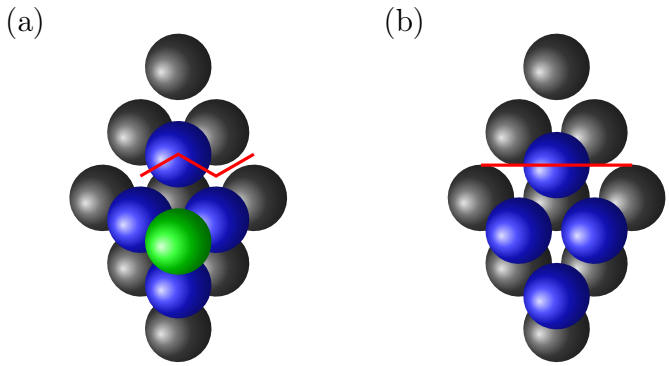

Figure 1.6: Sketch of the sliding layer state at high strains. (a) Registered motion with zig-zag trajectories, and (b) freely sliding layers.

At high strains the predominant structure is found to be registered sliding of hcp layers, for a sketch see fig. 1.6. Moreover, the dense direction of the hcp layer prefers to be parallel to the velocity at high strain amplitudes, whereas at low strains a dense direction is parallel to the flow direction. This behaviour results in a 30° turn in

the scattering pattern [101]. The corresponding diffraction patterns [100, 111] show three-fold symmetries. Besseling et al. have calculated an extensive nonequilibrium state diagram for hard spheres under oscillatory strain, which categorises further high-strain structures.

These structural transitions are connected to the rheological yielding process. The underlying mechanisms gain complexity with additional degrees of freedom of the colloids, which leads to novel phenomena. In recent years, there has been a focus on the yielding of colloidal glasses. A double yielding behaviour has been reported for hard sphere glasses [112] and attractive particles [113], which has been attributed to Brownian and shear induced cage escape processes leading to two maxima in the viscous modulus. Koumakis et al. have also been able to explain stress overshoots in the start-up shear experiment on hard sphere glasses [114]. A comprehensive rheological investigation on systems of spherical particles has demonstrated clearly that there is no such phenomenon [115] in hard sphere crystals. Turning to anisotropic particles, this feature has spurred interest in the role of translational-rotational coupling in the yielding process [116–118]. In fact, double yielding in the oscillatory strain sweep is observed in suspensions of dumbbell-shaped particles, characterised by two maxima at nearly the same stress value [115].

Goals and outline of this thesis In this thesis, the hard dumbbell system is investigated by means of BD simulations in and out of equilibrium. Strongly connected to recent experiments, the fundamental effects of anisotropic particles in colloidal suspension on material properties are elucidated.

First, the near-equilibrium response of hard dumbbell suspensions at small to intermediate aspect ratios is investigated to systematically understand the influence of the anisotropy on the microstructure and material properties. Of particular interest is the question at which elongation dynamic and structural properties start to deviate from the limiting hard sphere reference case. To clarify this question, we study the structure and fluctuations of suspensions of steeply repulsive dumbbell particles in equilibrium by means of BD computer simulations. We focus on the dense regime of the fluid to PC transition region of the phase diagram which is well accessible for experimental dumbbell suspensions and promises interesting insight into the influence of elongation on steric correlations and structural properties in both fluid and crystal. Apart from spatial correlations, we systematically explore the dynamic properties in the linear response regime at high volume fractions measured by equilibrium fluctuations. All results for the elongated dumbbells are discussed with respect to the well-explored hard sphere reference system.

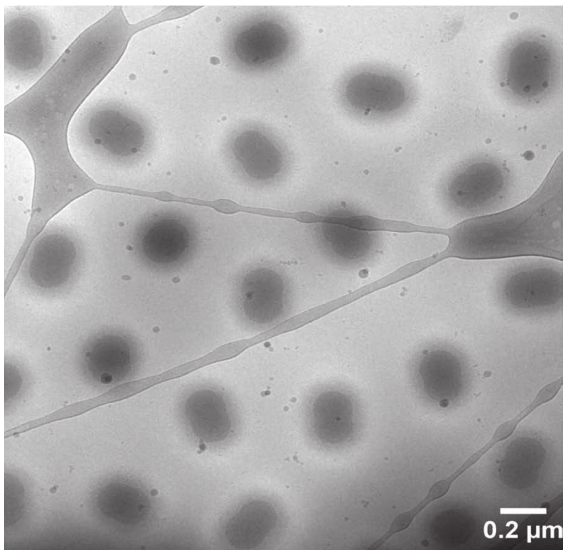

Figure 1.7: Cryogenic transmission electron micrograph of core-shell hard dumbbell colloids reprinted with permission from F. Chu, M. Siebenbürger, F. Polzer, C. Stolze, J. Kaiser, M. Hoffmann, N. Heptner, J. Dzubiella, M. Drechsler, Y. Lu, and M. Ballauff, Macromol. Rapid Commun. **33**, 1042–1048 (2012) [62]. Copyright © 2012, John Wiley & Sons. The particles' longest extent is about 600 nm, depending on the temperature, which can be used to tune the size of the shell.

The non-equilibrium behaviour is a challenge considering the huge parameter space and the complicated underlying phase diagram. In the non-equilibrium domain, our focus is on the region of small to moderate elongations (aspect ratios $L^* < 0.4$) and high volume fractions where the PC phase predominates [75]. The available data from experiments also falls into the interesting regions of the phase diagram where PCs are formed. Furthermore, kinetic properties of the suspensions are investigated in these simulations.

The recent, very clean experimental investigation [62, 119] of monodisperse hard dumbbells well matches the PC phase boundaries in the estimated phase diagram. Thanks to these advances, viable purely repulsive monodisperse model systems are experimentally available which crystallise in equilibrium conditions without the use of external fields or long-range interactions. Figure 1.7 shows micrograph of the core-shell dumbbells, which have been thoroughly studied at the aspect ratios 0.24 and 0.3. New scattering and rheology data on this system allow one to compare the simulation results with comprehensive experiments on the aspect ratios 0.24 and 0.3. The latter represents an anisotropy very close to that of a nitrogen molecule, which also features a PC phase [120, 121], referred to as the β-phase. Because of this, one could consider our system as *colloidal nitrogen*. Colloidal dumbbells are

thus among the most promising experimental model systems for a fundamental understanding of the structural and dynamic effects arising from increasing the elongation with respect to the hard sphere reference case. In particular, in the PC phase where new phenomena are expected [73].

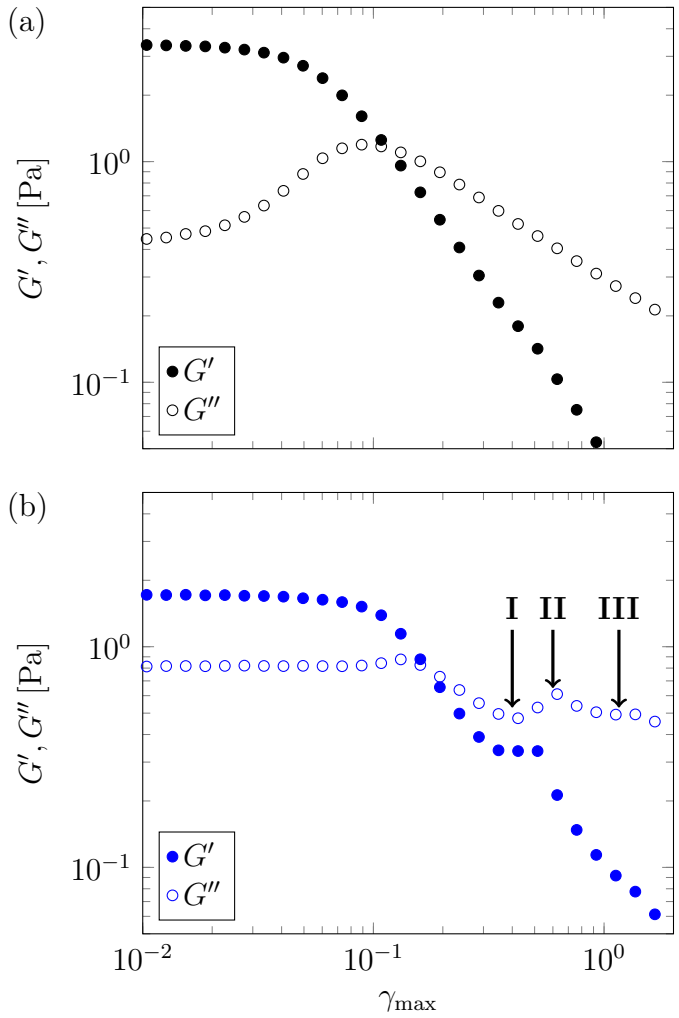

Figure 1.8: Dependence of storage moduli G' (filled circles) and loss moduli G'' (open circles) of hard spheres at $\phi_{\text{eff}} = 0.57$ (a) and hard dumbbells at $\phi_{\text{eff}} = 0.60$ (b) on increasing shear strains at a fixed frequency $f = 1\,\text{Hz}$. The strain positions (I), (II), (III) along the G curves indicate the strains connected to the respective structures discovered with SANS [115, 119]. Adapted with permission from F. Chu, N. Heptner, Y. Lu, M. Siebenbürger, P. Lindner, J. Dzubiella, and M. Ballauff, Langmuir **31**, 5992–6000 (2015) [115]. Copyright © 2015, American Chemical Society.

This allows us to compare the simulation results directly to a well-characterised experimental realisation. Oscillatory shear simulations of dense suspensions of

hard dumbbells reveal a partially oriented sliding layer state. This is a novel non-equilibrium state, which is similar to the well-known sliding layers of sheared hard spheres, showing an additional collective preference of orientation along the direction of flow. Our simulation data compares reasonably well to a rheo-SANS study of an experimental hard dumbbell system [115, 122]. This comparison shows that this novel transition is the cause for a vigorous rheological yielding behaviour depicted in fig. 1.8a, which features two distinct maxima of the viscous modulus G'' in an oscillatory strain sweep.

In this work, it is demonstrated that the origin of the double yielding is due to a structural transition as opposed to the cage-escape dynamics of the hard sphere glasses. Moreover, it is shown that the observed yielding process is due to structural rearrangement, sufficiently influenced by the mild anisotropy of the particles, whereas the hard sphere behaviour is retained for very small aspect ratios.

This thesis is organised as follows: first the theoretical framework, the numerical methods and a few strongly related experimental methods are introduced. In the main part the results regarding structure and dynamics from equilibrium and non-equilibrium simulations are presented. In the same section, experimental results [62, 115, 119, 122] are compared to the oscillatory shear BD simulations. In the last chapter, the results are summarised and discussed in the light of recommendable further research.

Chapter 2

Methods and theoretical framework

2.1 Fundamentals and numerical methods

In this chapter, we introduce the governing equations of motion for colloidal systems and important results from the literature, which are important for conduction and evaluation of computer simulations. These theories are equally important to understand related experimental measurements, which are briefly introduced in this chapter as well.

2.1.1 Equations of motion for colloidal particles

First, the equations of motion formulated in two different theoretical frames are briefly introduced. On this basis, the simulation methods and the particle interaction model are detailed.

Smoluchowski equation

The Smoluchowski equation describes the evolution of a N-particle density distribution $\rho^{(N)}(\mathbf{X}^N, t)$. In a compact form it reads

$$\frac{\partial}{\partial t}\rho^{(N)}(\mathbf{X}^N, t) = -\imath\mathcal{S}\rho^{(N)}(\mathbf{X}^N, t), \tag{2.1}$$

where $\mathcal{S}$ denotes the Smoluchowski operator and $\mathbf{X}^N$ and t refer to a set of phase-space coordinates and the time respectively [123]. The Smoluchowski operator can depend on interactions and external forces. In their absence, for the free diffusion of a particle with constant diffusivity D it reads $\mathcal{S} = \imath D\nabla^2$.

Langevin equation

The Langevin equation is the equation of motion for a particle of mass m immersed in volume filled with much smaller particles, we may write it as

$$m\ddot{\mathbf{r}}(t) = -m\xi\dot{\mathbf{r}}(t) + \mathbf{Z}(t), \tag{2.2}$$

where $\mathbf{r}(t)$ corresponds to a particle position. The inertia on the right-hand side (RHS) is balanced by a friction force counteracting the motion and a randomly fluctuating force $\mathbf{Z}(t)$. The magnitude of the friction is given by the friction coefficient ξ. For suspended Brownian particles it is determined by the solution of Stokes' equation [124, 125], which depends on the shape and the surface properties of the particle as well as the properties of the medium. In particular, the friction additionally depends on the full configuration of the system, which is the case for non-dilute suspensions of many particles. A hierarchy of clearly separated time scales is valid for Brownian particles. The first separation is already incorporated in eq. (2.4), which is reasonable if the Brownian particle is much larger than the surrounding solvent particles. In this case, the collisions of solvent particles with the Brownian solute are δ-correlated in time. If the friction force dominates the dynamics of the particle, the ballistic motion decays virtually instantaneously, such that the motion is determined by the fluctuating force and the friction force only. This regime is the so-called overdamped or Brownian dynamics, in which the inertia term (left-hand side (LHS) of eq. (2.2)) is negligible. A common approximation to the many-body hydrodynamic problem is to neglect hydrodynamic interactions, reducing the friction tensor to a constant as in the single particle problem. The random force is assumed to be undirected, thus its mean vanishes

$$\langle \mathbf{Z}(t) \rangle = 0, \tag{2.3}$$

where the angle brackets $\langle \dots \rangle$ denote the time average. In the Langevin case the random process is δ-correlated, i.e. it is memoryless in the sense that only the current state of the system is relevant for its future evolution. The autocorrelation function of the random process can be written as

$$\langle \mathbf{Z}(t+t') \cdot \mathbf{Z}(t') \rangle = 2\pi Z_0 \delta(t), \tag{2.4}$$

where Z_0 is a constant.

As opposed to the Smoluchowski theory, which predicts the density distribution of a system, the Langevin dynamics describes the evolution of single particle's positions and velocities. For Brownian particles with position-independent diffusion coefficients the Langevin and Smoluchowski dynamics are equivalent [126].

Fluctuation-dissipation relation

The relation of the dissipative and stochastic forces in eq. (2.2) is expressed in a fluctuation-dissipation relation

$$k_{\mathrm{B}}T\xi = \frac{\pi Z_0}{3m}, \tag{2.5}$$

where T is the temperature. Asymptotically, the mean-square displacement of eq. (2.2) at very large times grows linearly as

$$\left\langle |\mathbf{r}(t)|^2 \right\rangle \simeq 6\frac{k_B T}{\xi m}t, \tag{2.6}$$

where the diffusion coefficient is defined as

$$D = \frac{k_B T}{\xi m} \tag{2.7}$$

and k_B and T denote the Boltzmann constant and the temperature respectively. A well-known representative is the Stokes-Einstein relation for spherical particles of diameter d with no-slip boundary conditions is

$$D_0^S = \frac{k_B T}{3\pi\eta d}, \tag{2.8}$$

in a medium with viscosity η. Which relates the dissipation due to Stokes friction to its Brownian mobility due to thermal fluctuations. For particles with different geometries or boundary conditions this relation has to be generalised [125, 127–129]. The calculation of the Stokes friction and the associated diffusivities for the particles considered in this work is detailed in section 2.1.5.

2.1.2 Dumbbell model and pairwise interaction

A hard dumbbell particle is comprised of two fused spheres (fig. 2.1), which are considered as centres of interaction in our model. The beads of diameter d are rigidly constrained at a centre-to-centre distance L, see Fig. 2.1. With that we define a dimensionless elongation L^*, or, aspect ratio, defined as $L^* = L/d$. For $L^* = 0$, we recover the reference case of one spherical colloid.

The purely excluded volume interaction is step function, which is infinitely repellent at overlap of two distinct particles and zero elsewhere. For numerical and practical reasons, one typically chooses a smooth potential. The site-site (bead-bead) pair interaction is modelled by a Yukawa potential, which is the electrostatic part of the well-known Derjaguin-Landau-Verwey-Overbeek (DLVO) theory [130]. In the present simulations the Yukawa potential is used because of it can be used

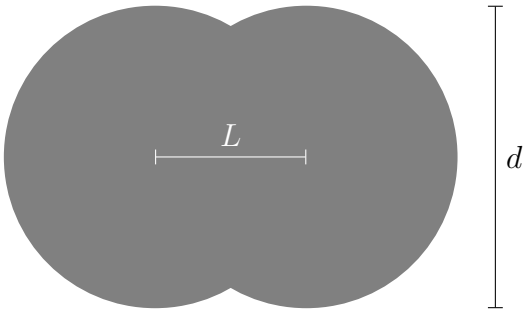

Figure 2.1: Sketch of the dumbbell geometry with dimensionless aspect ratio $L^* = L/d$.

to interpolate between long-range electrostatic repulsion and steep hard-core like repulsion by tuning the screening parameter κ. There are other potential forms considered for modelling the hard-core interaction in the literature as well, inverse power potentials are also quite common [131].

The potential between two beads at distance r is given by

$$V(r) = \epsilon \frac{\sigma}{r} \exp\left\{-\kappa\left(r-\sigma\right)\right\}. \tag{2.9}$$

The parameter κ is a screening constant, which may be used to tune the softness of the pair interaction. In the limit of $\kappa \to \infty$ one obtains the purely hard-core interaction. We choose $\kappa = 20/\sigma$ as a compromise between a steep hard-core like repulsion at the same time being smooth enough to not cause numerical problems in the integration. The parameters σ and $\epsilon = k_B T$ define the length and energy scale of the interaction in our model, respectively. In order to fit the important colloidal volume fraction parameter to the hard system, one may define an effective volume fraction taking into account the excluded volume caused by the repulsive interaction. Since we compare our results to the hard-dumbbell and hard-sphere reference system, we define the effective bead diameter d via the Barker-Henderson relation [132]

$$d = \int_0^\infty (1 - \exp\{-\frac{V(r)}{k_B T}\})\mathrm{d}r. \tag{2.10}$$

The effective volume fraction $\phi = \rho(\pi/6)\alpha(L^*)d^3$ at dumbbell number density ρ is defined accordingly. The function $\alpha(L^*) = 1 + 3L^*/2 - L^{*3}/2$ is a geometric factor accounting for the bead overlap volume [75].

2.1.3 Brownian dynamics

Based on the Langevin dynamics in the overdamped case, Brownian dynamics (BD) simulations for pair-wise interacting particles are carried out in this work. First,

the method for the equilibrium simulations is described. This is followed by the method employed for a shear set-up along with the properties of the induced flow. The implementation of this method can be found in the appendix section A.3.

Equilibrium

The total instantaneous force $\mathbf{F}_{ij}(t)$ exerted by particle j on particle i is the sum of the forces $\mathbf{F}_{(i,k)(j,l)}(t)$ acting between the k-th site of the i-th particle and the l-th site of the j-th particle, via

$$\mathbf{F}_{ij}(t) = \sum_{k,l=1}^{2} \mathbf{F}_{(i,k)(j,l)}(t). \tag{2.11}$$

The centre of mass (COM) vector of the i-th particle is decomposed with respect to the axial symmetry as

$$\mathbf{R}_i(t) = \mathbf{R}_{i,\perp}(t) + \mathbf{R}_{i,\parallel}(t), \tag{2.12}$$

$$\mathbf{R}_{i,\parallel}(t) = \left[\mathbf{u}_i(t) \cdot \mathbf{R}_i(t)\right] \mathbf{u}_i(t), \tag{2.13}$$

where $\mathbf{u}_i(t)$ is the unit vector pointing in the direction of the connection between the centres of the beads belonging to the i-th particle. The total force $\mathbf{F}_i(t)$ is decomposed analogously: The parallel and perpendicular parts are given by

$$\mathbf{F}_i(t) = \mathbf{F}_{i,\perp}(t) + \mathbf{F}_{i,\parallel}(t), \tag{2.14}$$

$$\mathbf{F}_{i,\parallel}(t) = \left[\mathbf{u}_i(t) \cdot \mathbf{F}_i(t)\right] \mathbf{u}_i(t). \tag{2.15}$$

Given this framework, we implement the BD algorithm for the above defined coordinates as follows: The particle positions are updated using an explicit forward Euler method with the finite time step $\Delta t \ll \tau$. Starting from the configuration $\{\mathbf{R}_i^n, \mathbf{u}_i^n\}$ at time $t = n\Delta t$, we find new coordinates $\left\{\mathbf{R}_i^{n+1}, \mathbf{u}_i^{n+1}\right\}$ at $t+\Delta t$ following the scheme

$$\mathbf{R}_{i,\parallel}^{n+1} = \mathbf{R}_{i,\parallel}^{n} + \Delta t \frac{D_\parallel}{k_\mathrm{B}T} \mathbf{F}_{i,\parallel}^{n} + \delta r_{i,\parallel} \mathbf{u}_i^n, \tag{2.16}$$

$$\mathbf{R}_{i,\perp}^{n+1} = \mathbf{R}_{i,\perp}^{n} + \Delta t \frac{D_\perp}{k_\mathrm{B}T} \mathbf{F}_{i,\perp}^{n} + \delta r_{i,1} \mathbf{e}_{i,1}^n + \delta r_{i,2} \mathbf{e}_{i,2}^n, \tag{2.17}$$

where $\mathbf{e}_{i,1}$ and $\mathbf{e}_{i,2}$ are unit vectors oriented perpendicular to the director $\mathbf{u}_i$. The random variates $\delta r_{i,\alpha},\ \alpha \in \{\|, 1, 2\}$ have zero mean and the variances $\left\langle \delta r_{i,\|}^2 \right\rangle = 2D_\parallel \Delta t$ and $\left\langle \delta r_{i,\{1,2\}}^2 \right\rangle = 2D_\perp \Delta t$, respectively.

The torque acting on symmetric dumbbells is given by $\mathbf{T}_i(t) = \frac{\sigma}{2} L^* \mathbf{u}_i(t) \times \left(\mathbf{F}_{(i,2),\perp}(t) - \mathbf{F}_{(i,1),\perp}(t)\right)$, where $\mathbf{F}_{(i,k),\perp}(t)$ is the total instantaneous force on the

k-th bead of the i-th particle. The internal unit director $\mathbf{u}_i$ of the i-th particle is updated according to

$$\mathbf{u}_i^{n+1} = \mathbf{u}_i^n + \Delta t \frac{D_r}{k_\mathrm{B}T} \mathbf{T}_i^n \times \mathbf{u}_i^n + \delta x_1 \mathbf{e}_{i,1}^n + \delta x_2 \mathbf{e}_{i,2}^n, \tag{2.18}$$

where δx_1 and δx_2 are zero mean Gaussian distributed random variates with variance $\langle \delta x_j^2 \rangle = 2D_r \Delta t$. The single particle mobility is given by parallel $D_\parallel$, perpendicular $D_\perp$ and rotational D_r diffusion coefficients. The time scale is set to the Brownian time $\tau = \sigma^2/D_0^S$ of a single bead of diameter σ and diffusivity $D_0^S = k_B T(3\pi\eta_s\sigma)^{-1}$ with a solvent viscosity η_s. We neglect hydrodynamic interactions between the colloids which is justified for the high packing fractions where steric correlations dominate the equilibrium structure and linear response behaviour [133, 134].

Shear conditions

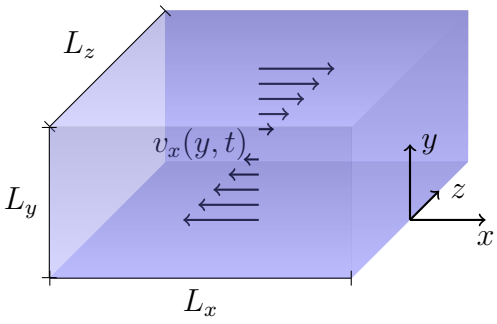

Figure 2.2: Sketch of the simulated box under shear flow. The flow velocity $v_x(y,t)$ has a linear gradient $\dot{\gamma}(t)$ in y-direction. In out specific case, the flow varies sinusoidal in time. The dimensions of the box are L_x, L_y, L_z. Reprinted with permission from N. Heptner, F. Chu, Y. Lu, P. Lindner, M. Ballauff, and J. Dzubiella, Phys. Rev. E **92**, 052311 (2015) [122]. Copyright © 2015, American Physical Society.

As for the equilibrium simulations, we employ a forward Euler scheme in order to integrate the equations of motion [42, 135]. In fig. 2.2 the basic set-up for sheared simulations is sketched. The parallel and perpendicular COM coordinates are also updated according to eqs. (2.16) and (2.17). Here, the shear flow with the time-dependent shear rate $\dot{\gamma}(t)$ only affects the COM transport in x-direction through the last term in

$$\mathbf{R}_i^{n+1} = \mathbf{R}_{i,\parallel}^{n+1} + \mathbf{R}_{i,\perp}^{n+1} + \Delta t \dot{\gamma}(t) R_y^n \mathbf{e}_x. \tag{2.19}$$

The directors are updated following

$$\mathbf{u}_i^{n+1} = \mathbf{u}_i^n + \Delta t \frac{D_r}{k_\mathrm{B}T}\mathbf{T}_i^n \times \mathbf{u}_i^n + \delta x_1 \mathbf{e}_{i,1}^n + \delta x_2 \mathbf{e}_{i,2}^n, \tag{2.20}$$

where $\mathbf{T}_i^n$ is the total torque exerted on particle i at time $t = n\Delta t$. The torque is comprised of the inter-particle and background-flow contributions.

$$\mathbf{T}_i(t) = \mathbf{T}_i^p(t) - \frac{k_B T}{D_r}\left\{\mathbf{u}_i(t) \times E(t) \cdot \mathbf{u}_i(t)\right\} \tag{2.21}$$

We impose simple shear flow given by the rate-of-strain tensor

$$E(t) = \dot{\gamma}(t) \begin{pmatrix} 0 & 1 & 0 \\ 0 & 0 & 0 \\ 0 & 0 & 0 \end{pmatrix}, \tag{2.22}$$

which may be written as a sum of symmetric and anti-symmetric tensors, i.e. the shear and vorticity tensors

$$E(t) = \Gamma(t) + \Omega(t) \tag{2.23}$$

$$= \frac{1}{2}\dot{\gamma}(t) \begin{pmatrix} 0 & 1 & 0 \\ 1 & 0 & 0 \\ 0 & 0 & 0 \end{pmatrix} + \frac{1}{2}\dot{\gamma}(t) \begin{pmatrix} 0 & 1 & 0 \\ -1 & 0 & 0 \\ 0 & 0 & 0 \end{pmatrix}. \tag{2.24}$$

The symmetric part Γ describes the pure elongational flow, while the anti-symmetric part Ω describes the vorticity of the flow. The vorticity is spatially uniform and quantifies the solvent contribution to the rotation of the particles.

Above, the form of the time evolution of the shear field is not specified. In the oscillatory shear set-up, the time-dependent dimensionless strain imposed by the flow field on the suspension is given by

$$\gamma(t) = \gamma_{\max} \sin(2\pi f t). \tag{2.25}$$

Thus, the linear solvent velocity profile is

$$v_x(y,t) = \dot{\gamma}(t) y, \tag{2.26}$$

where the shear rate $\dot{\gamma}(t)$ is the time-derivative of the strain $\gamma(t)$ with the amplitude $\gamma_{\max}$ and the frequency f. The maximum shear rate $\dot{\gamma}_{\max}$ sets the time scale of the driving force exerted by the shear flow. In order to compare the driving force to the intrinsic viscous forces, we define the Péclet numbers

$$\mathrm{Pe} = \frac{1}{12} f \gamma_{\max} \sigma^2 / D_0^S = \frac{1}{12} f \gamma_{\max} \tau, \text{ and} \tag{2.27}$$

$$\mathrm{Pe}_r = 2\pi f \gamma_{\max} / D_r, \tag{2.28}$$

where the latter is a definition respecting the time scale set by the rotational Brownian motion.

2.1.4 Shear boundary conditions

The usual periodic boundary conditions (PBC) have to be modified in order to be compatible with the imposed shear field. A solution to this requirement is Lees-Edwards boundaries [136]. There are two different representations of these boundary conditions, which may be fulfilled by an inclined simulation box or *sliding images*, here we introduce the latter shown in fig. 2.3. When a particle leaves the central image's boundary in the shear gradient direction, it is inserted at the opposite boundary with a separation in flow direction according to the current shear state. If these boundary conditions are implemented for time-independent

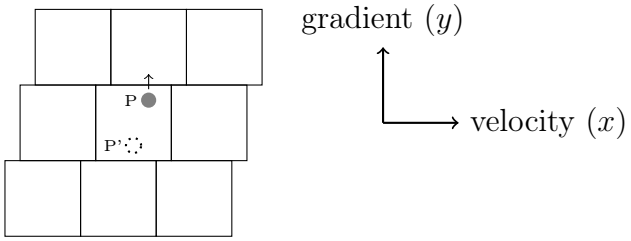

Figure 2.3: Sketch of Lees-Edwards periodic shear boundaries. The particle at point P leaving the central image is inserted at point P' with a displacement due to the flow.

flow, the simulated system reaches a steady shear state after sufficient time [137]. In this work, the Lees-Edwards boundary conditions are used in combination with an imposed background velocity field according to eq. (2.25), which may depend on time as described above.

2.1.5 Calculation of the single-particle diffusivities

The infinite-dilution (single-particle) self-diffusion coefficients of a dumbbell particle are calculated using the shell-bead model (SHM) [127, 138–141], the relevant values are summarised in table 2.1. This hydrodynamic model is based on a Rotne-Prager-Yamakawa (RPY) tensor level solution of Stokes' equation for the flow past a dumbbell [124]. The RPY-Tensor is a generalisation of the Oseen-Tensor, which is the Greens function of the Stokes equation for a singular force acting on the medium. In this method, the particle surface is represented by a number of mini-beads which act as sources of hydrodynamic friction For each of these small spheres, the Stokes flow is known. We assume no-slip boundaries, which means that the velocity of the medium is equal to the respective surface's velocity at the boundaries. Using these known solutions, the values are extrapolated to zero mini-bead size, e.g., infinite

L^*	$D_\parallel/D_0^S$	$D_\perp/D_0^S$	D_r/D_r^S
0.02 (S)	0.99	0.99	0.97
0.10 (C)	0.97	0.95	0.85
0.24 (A)	0.93	0.89	0.69
0.30 (B)	0.91	0.87	0.63

Table 2.1: Single particle diffusive properties used in the simulations, obtained by SHM calculations.

number of friction sources on the particle surface. We are using the parallel $D_\parallel/D_0^S$, perpendicular $D_\perp/D_0^S$ and rotational D_r/D_r^S diffusion coefficients obtained by the above method as input for the presented BD simulations. The free single-sphere ($L^* = 0$) translational D_0^S and rotational D_r^S diffusivities are be obtained from the respective Stokes-Einstein relations [125]. The translational COM diffusion coefficient of a free dumbbell is given by $D_0 = \frac{1}{3}D_\parallel + \frac{2}{3}D_\perp$. Here, the Brownian time is accordingly given by $\tau = \sigma^2/D_0^S$ [42, 142].

More values are presented in section A.2 in the appendix.

2.1.6 Numerical details

Equilibrium simulations

In our simulations, the systems have PBC in all three Cartesian dimensions in a cubic box with $L_x = L_y = L_z$. The presented results have been obtained from BD simulation runs with $N = 864$ particles in a constant volume V, so that the number density $\rho = N/V$. The total simulation time is 130τ with the time step of $\Delta t = 10^{-4}\tau$. The face-centered cubic (fcc) ordered COMs with directors pointing in the $(1, 1, 1)$ directions have been set as initial configuration. To ensure equilibrium conditions results have only been obtained for $t \geq 50\tau$. All statistical correlations have been calculated for $50\tau < t < 100\tau$ using every 100-th time step.

Non-equilibrium simulations

We simulate ($N = 864$) dumbbell particles subjected to Lees-Edwards [136] periodic boundary conditions. The systems are initialised in a crystalline state and run for 100τ, at the frequencies $f = 1\tau^{-1}$, $f = 3\tau^{-1}$ and $f = 5\tau^{-1}$. The time step is set to $10^{-4}\tau$, $5 \cdot 10^{-5}\tau$ or $2.5 \cdot 10^{-5}\tau$ depending on the strain amplitude which also sets the maximum shear rate and, thus, the time scale of the shearing motion. The box is shaped such that it supports the hexagonal layer structure. The simulations

are run for 100τ and the trajectories are analysed after reaching the steady state, earliest after 50τ of running time. The averages are calculated over 50 and 250 strain cycles in the steady state respectively. Figure 4.5 shows the parameters we have investigated in oscillatory shear conditions and the states we have identified. For a summary of the equilibrium state points under consideration the reader is referred to fig. 4.1.

2.2 Simulation analysis

2.2.1 Spatial structure

Here, the measures to probe the spatial structure of the suspensions are summarised. This includes spatial correlation functions as well as order parameters to quantify orientational and translational order. In particular, the scattering intensities can be compared directly to experimental results.

Pair correlation functions

Site-site radial distribution function The radial distribution function (RDF) of the individual sites is defined as

$$g_s(\mathbf{r}) = \frac{1}{N\rho} \left\langle \sum_k \sum_l \delta\left(\mathbf{r} - (\mathbf{r}_k - \mathbf{r}_l)\right) \right\rangle, \tag{2.29}$$

where the indices k and l run over all beads. This correlation function is connected to collision rates in the Enskog theory, which is introduced in 2.2.2.

Expansion of the RDF The RDF, which describes spatial correlations of pairs of particles, is connected to the structure factor $S(q)$ via a Fourier transform, where q is the magnitude of the wave vector. For a system of anisotropic particles the pair correlation function may be expanded into spherical harmonics separating the COM and orientational correlations. The expansion of the full RDF [143] yields two partial correlation functions of particular interest: We calculate the radial distribution function of the COMs

$$g(r) = \frac{1}{\rho N} \left\langle \sum_{i \neq j}^{N} \delta\left(\mathbf{r} - \mathbf{R}_{ij}\right) \right\rangle, \tag{2.30}$$

and the orientational radial distribution function

$$g_{P_2}(r) = \frac{1}{\rho N g(r)} \left\langle \sum_{i \neq j}^{N} P_2\left(\cos\theta_{ij}\right) \delta\left(\mathbf{r} - \mathbf{R}_{ij}\right) \right\rangle, \tag{2.31}$$

where $\mathbf{R}_{ij}$ denotes the COM separation vector of the i-th and j-th particles, and θ_{ij} is the angle between the respective directors. The orientational distribution function $g_{P_2}(r)$ describes the spatial correlation of the particle directors with P_2 denoting the second Legendre polynomial, it is therefore not able to distinguish parallel and antiparallel configurations. The function $g_{P_2}(r)$ equals 1 for parallel aligned particles, $-\frac{1}{2}$ for perpendicular alignment and vanishes for uncorrelated orientations.

Structure factors

The structure factor $S(q_x, q_z)$ is evaluated in the plane $q_y = 0$. This reciprocal plane corresponds to a neutron experiment where the incident beam is parallel to the gradient direction of the shear flow. We calculate the structure factor directly from the COM coordinates as

$$S(q_x, q_z, 0) = \left\langle \sum_{i=1}^{N} e^{-\imath \mathbf{q}\cdot\mathbf{R}_i} \right\rangle . \tag{2.32}$$

Scattering intensity

In order to compare to experimental scattering results, we calculate the intensity distribution for the simulated systems. The scattering intensity of the suspension $I(\mathbf{q})$ is the convolution of the COM structure and the distribution of scattering centres within each particle. The scattering function depends on the exact shape, composition and density of the colloidal particles in addition to the colloidal structure and orientation. For simplicity reasons, our analysis is restricted to a constant internal density of the dumbbell particles. If one additionally assumes a flat distribution of orientations it is possible to separate the so called form factor $P(q)$ from the structure factor $S(\mathbf{q})$. The scattering amplitude $A(\mathbf{q};\mathbf{u})$ describes the scattering of a single particle with orientation $\mathbf{u}$ and constant internal density at the scattering vector $\mathbf{q}$. Averaging the scattering amplitudes over all possible orientations yields the form factor $P(q)$. The total scattering intensity is calculated as

$$I(\mathbf{q}) = \left\langle \sum_{j,l} A(\mathbf{q};\mathbf{u}_l) A(\mathbf{q};\mathbf{u}_j) e^{-\imath \mathbf{q}\cdot(\mathbf{R}_l - \mathbf{R}_j)} \right\rangle , \tag{2.33}$$

where the scattering amplitude of a homogeneous dumbbell tilted by the angle θ with respect to the scattering vector $\mathbf{q}$ is given by [144]

$$A(\mathbf{q};\mathbf{u}) = 4\pi R^3 \int_{-L^*}^{1} dt \cos\left(q\cos\theta R\left[t+L^*\right]\right). \tag{2.34}$$

The code used to calculate eq. (2.33) is listed in the appendix section A.4.

Orientation

In order to analyse the orientational behaviour of the particles, a measure of the orientation respecting the geometry of the system given is used. The measure we choose is closely related to the well-known nematic order parameter employed in the literature. We plot the mean orientation with respect to the Cartesian axes, which coincide with the velocity (x), shear gradient (y) and vorticity axes (z), as

$$\langle P_2^{\alpha}\rangle_{\text{cycle}}(t) = \langle P_2(\cos\theta_{\alpha})\rangle_{\text{cycle}}(t), \tag{2.35}$$

where α are the coordinates x, y, z and $\theta_{\alpha}(t)$ the corresponding instantaneous angles. The average $\langle\dots\rangle_{\text{cycle}}$ denotes sampling all time steps with the imposed strain state $\gamma(t)$.

COM order parameters

In this work, local bond order measures are used to probe the state of the system. The ensemble average of the locally calculated structural values yields a viable method to investigate the type and quality of the overall structure of the system. The method may as well be used to investigate the distribution of nuclei or the propagation of nucleation phenomena [78]. In order to distinguish crystalline structures we use the local bond order analysis proposed by [145]. For each particle i a vector $\mathbf{q}_l(i)$ is defined by the components

$$q_{lm} = \frac{1}{N_b(i)} \sum_{j=1}^{N_b(i)} Y_{lm}(\hat{\mathbf{R}}_{ij}), \tag{2.36}$$

where $Y_{lm}(\hat{\mathbf{R}}_{ij})$ are the spherical harmonics for the normalised separation vectors $\hat{\mathbf{R}}_{ij}$, and $N_b(i)$ is the number of the i-th particle's neighbours.

$$\overline{q}_l(i) = \frac{4\pi}{2l+1} \sum_{m=-l}^{l} \left|q_{lm}(i)\right|^2, \tag{2.37}$$

$$\overline{w}_l(i) = \left(\sum_{m=-l}^{l} |q_{lm}(i)|^2 \right)^{-3/2} \times \sum \begin{pmatrix} l & l & l \\ m_1 & m_2 & m_3 \end{pmatrix} q_{lm_1}(i) q_{lm_2}(i) q_{lm_3}(i), \tag{2.38}$$

where the second sum runs over all $-l \leq m_j \leq l$ fulfilling $m_1 + m_2 + m_3 = 0$.

We define the ensemble averaged order parameters as

$$\langle Q_l \rangle = \left\langle \frac{1}{N} \sum_{i=1}^{N} \overline{q}_l(i) \right\rangle, \text{ and} \tag{2.39}$$

$$\langle W_l \rangle = \left\langle \frac{1}{N} \sum_{i=1}^{N} \overline{w}_l(i) \right\rangle, \tag{2.40}$$

where the angle brackets $\langle \dots \rangle$ denote the time average in the steady state. In this work the COM order is monitored in terms of averaged local order parameters Q_4 and W_4. These order parameters are sensitive to the configurations of the neighbourhoods of solid-like particles. In particular, fcc and hexagonal close packed (hcp) structures are separated by a change of the sign of W_4.

2.2.2 Dynamical properties

In the following, the methods to investigate the dynamics of the systems are described in a compact form.

Linear response theory

Dynamical properties of a system may be obtained from fluctuations in equilibrium, i.e. the response to an external field can be determined in an unperturbed system. These Green-Kubo type relations [146, 147], which result from a linearisation of the Smoluchowski equation for a perturbed system, are valid for very small perturbations of the equilibrium state on short time scales [123, 148]. In the following, linear response theory is used to calculate dynamical properties of hard dumbbell suspensions from BD simulation trajectories.

Translational diffusion

We calculate the translational diffusion in the linear response regime from Green-Kubo-type of relations. In the limit of linear response, we thus obtain the long-time COM self-diffusion coefficient D_s^L from the time correlation functions in equilibrium

from the integral of the velocity autocorrelation function (VACF) as

$$D(t) = \int_0^t \langle \mathbf{V}(0) \cdot \mathbf{V}(t') \rangle \, \mathrm{d}t', \tag{2.41}$$

where $\mathbf{V}(t)$ is the instantaneous COM velocity. The long-time limit of this function is the long-time self-diffusion coefficient

$$D_s^L = \lim_{t \to \infty} D(t). \tag{2.42}$$

We define the mean square displacements (MSDs) of the COM $W_c(t)$, parallel $W_\parallel(t)$ and perpendicular $W_\perp(t)$ with respect to the initial orientation $\mathbf{u}(0)$ as

$$W_c(t) = \frac{1}{N} \left\langle \sum_{i=1}^{N} \Delta \mathbf{R}_i^2(t) \right\rangle, \tag{2.43}$$

$$W_\parallel(t) = \frac{1}{N} \left\langle \sum_{i=1}^{N} \Delta \mathbf{R}_{i,\parallel}^2(t) \right\rangle, \tag{2.44}$$

$$W_\perp(t) = \frac{1}{N} \left\langle \sum_{i=1}^{N} \Delta \mathbf{R}_{i,\perp}^2(t) \right\rangle. \tag{2.45}$$

The displacements of the COM, the parallel and the perpendicular coordinates are defined as

$$\Delta \mathbf{R}_i(t) = \mathbf{R}_i(t) - \mathbf{R}_i(0), \tag{2.46}$$

$$\Delta \mathbf{R}_{i,\parallel}(t) = \left[\mathbf{u}_i(0) \cdot \Delta \mathbf{R}_i(t) \right] \mathbf{u}_i(0) \text{ and} \tag{2.47}$$

$$\Delta \mathbf{R}_{i,\perp}(t) = \Delta \mathbf{R}_i(t) - \Delta \mathbf{R}_{i,\parallel}(t), \tag{2.48}$$

respectively. With that, the time-dependent diffusion coefficients in the particle reference frame are then given by

$$D_c(t) = \frac{1}{6t} W(t), \tag{2.49}$$

$$D_\parallel(t) = \frac{1}{2t} W_\parallel(t), \tag{2.50}$$

$$D_\perp(t) = \frac{1}{4t} W_\perp(t). \tag{2.51}$$

The long-time limit of the self-diffusion coefficients for $\alpha \in \{c, \parallel, \perp\}$ is obtained from the MSD data as

$$D_\alpha^L = \lim_{t \to \infty} D_\alpha(t). \tag{2.52}$$

Orientational relaxation

The linear response orientational relaxation is quantified in terms of the directional autocorrelation function (DACF) defined as

$$C_{\mathbf{u}}(t) = \langle \mathbf{u}(0) \cdot \mathbf{u}(t) \rangle = e^{-2D_r(t)t}. \tag{2.53}$$

We assume that the particle orientations become diffusive for long times with the constant D_r^L, therefore asymptotically the following relation holds [142]:

$$C_{\mathbf{u}}(t) = e^{-2D_r^L t}. \tag{2.54}$$

Similarly [149], we define an effective decay time τ_r for the non-equilibrium steady-state case

$$C_1(t) = \langle \mathbf{u}(0) \cdot \mathbf{u}(t) \rangle = e^{-2\frac{t}{\tau_r}}. \tag{2.55}$$

Shear viscosity

In the limit of zero strain, we may obtain the dynamic viscosity of the suspension from equilibrium fluctuations. In particular, we calculate the relative dynamic viscosity difference from the off-diagonal stress autocorrelation function (SACF)

$$z_{\alpha\beta}(t) = \frac{1}{V k_{\mathrm{B}} T} \langle \sigma_{\alpha\beta}(0) \sigma_{\alpha\beta}(t) \rangle , \tag{2.56}$$

where the symmetric stress tensor is defined as

$$\sigma_{\alpha\beta} = \frac{1}{V} \sum_{i=1}^{N} \sum_{j>i}^{N} r_{ij\alpha} F_{ij\beta}, \tag{2.57}$$

and $\alpha \neq \beta$ denote Cartesian components. From our BD simulations, the potential part of the stress tensor is available, therefore (2.57) does not contain a momentum part.

The steady shear viscosity difference is obtained from the integral of the SACF as

$$\eta_0 = \int_0^\infty z_{\alpha\beta}(t) \mathrm{d}t. \tag{2.58}$$

Radial distribution function and Enskog collision rate

In a homogeneous and isotropic system the site-site RDF depends only on the distance $r = |\mathbf{r}|$. The Enskog collision rate for hard spheres with diameter σ_{HS} is given by

$$\Gamma_E = g(\sigma) \Gamma_0, \tag{2.59}$$

where $g(\sigma)$ is the contact value of the RDF and Γ_0 is the collision frequency in the dilute gas which is the ratio of the mean velocity and the free path in a suspension of hard spheres. In the Enskog approximation, which neglects correlated collisions, the self-diffusion coefficient is inversely proportional to the contact value of the radial distribution function

$$D_E = \frac{3k_BT}{2m\Gamma_E}. \tag{2.60}$$

2.3 Related experimental techniques

In this section a number of experimental methods are discussed, which are relevant to the systems under consideration in this work and have been employed by co-workers.

2.3.1 Light scattering and particle mobility

In a dilute system of colloidal particles, light scattering methods may be used to determine the single-particle mobility, and, with the use of a hydrodynamic model, the shape of the particle [150, 151]. The intensity autocorrelation function (ACF) of light scattered by a volume containing a dilute suspension of Brownian particles can be related to the mean square displacement of the centres of masses and appropriate axes of rotation. As the intensity ACF is proportional to the density ACF and the Smoluchowski theory is applicable to the dilute system, we can connect the observable to the microscopic density. This is expressed in the Siegert relation

$$g_I(\mathbf{q}, t) = 1 + \left|g_E(\mathbf{q}, t)\right|^2, \tag{2.61}$$

where $\mathbf{q}$ represents the scattering vector, t the time lag, g_I and g_E are the normalised intensity and electric field ACFs, respectively. The electric field ACF is proportional to an exponential with a polynomial of the characteristic times of the translational and orientational motion as argument. In dynamic light scattering experiments the information that is available from the intensity correlation function depends on the specific scattering geometry, which can be dynamic light scattering (DLS) or depolarised dynamic light scattering (DDLS).

For linear molecules the intensity ACF of parallel-polarised light in the vertical (vv) geometry is proportional to

$$g_I^{vv}(\mathbf{q}, t) \propto \left\{\alpha^2 + \frac{4}{45}\beta^2 e^{-6D_r t}\right\} e^{-q^2 D_0 t}, \tag{2.62}$$

and the correlation function for the perpendicularly polarised scattering in the vertical-horizontal (vh) geometry reads

$$g_I^{vh}(\mathbf{q},t) \propto \beta^2 e^{-6D_r t} e^{-q^2 D_0 t}, \tag{2.63}$$

where α and β are the mean polarisability and the polarisability difference regarding the parallel and arbitrary perpendicular axes of the linear particle.

If a hydrodynamic model of the particle is available as well, the decay times of the intensity correlation functions can be related to the mobility matrix of this model. In section 2.1.5 the employed model for the calculation of the mobility matrix is described. The exact morphology of the colloidal particles is important with respect to our modelling in BD simulations and the determination of the equilibrium states of the experimental samples. The latter are the effective volume fraction ϕ_{eff} and elongation of the particles depicted in fig. 2.4. Figure 2.4a shows the fraction of crystallised sample upon crossing the coexistence region or $L^* = 0.3$. The boundaries of this region are plotted in fig. 2.4b for the elongations $L^* = 0.24$ and 0.3 along with the prediction [77] of the phase diagram. This comparison to the prediction of the phase diagram by Monte Carlo (MC) simulations [77] shows that the coexistence region (fluid/plastic crystal (PC)) shrinks on increasing elongation and the phase boundaries of the experimental systems at $L^* = 0.24$ and 0.3 fit very well to the prediction (see fig. 2.4).

2.3.2 Small-angle neutron scattering

Small-angle neutron scattering (SANS) may be used as a tool to investigate the structure of a sample under a great number of conditions. Since neutrons, which have very short wavelengths, are scattered at the atomic nuclei, colloidal suspensions are basically transparent, such that multiple scattering occurs rarely and dense systems can be investigated. In particular rheo-SANS set-ups allow to observe systems under shear conditions [53]. In these experiments the neutron beam goes through the shear cell in certain directions to learn about the structure of the sample. The shear flow breaks the isotropy of the system, such that three directions are important. These are the velocity (x), the velocity gradient (y) and the vorticity (z) directions in the case of simple shear (cf. section 2.1.3). There are certain geometries in rheo-SANS experiments, which coincide with the observation of prominent planes of the shear flow. For the radial geometry depicted in fig. 2.5, the neutron beam is aligned with the velocity gradient of the flow, such that scattering from the velocity-vorticity plane may be observed. In the tangential geometry, the incident beam is parallel to the velocity.

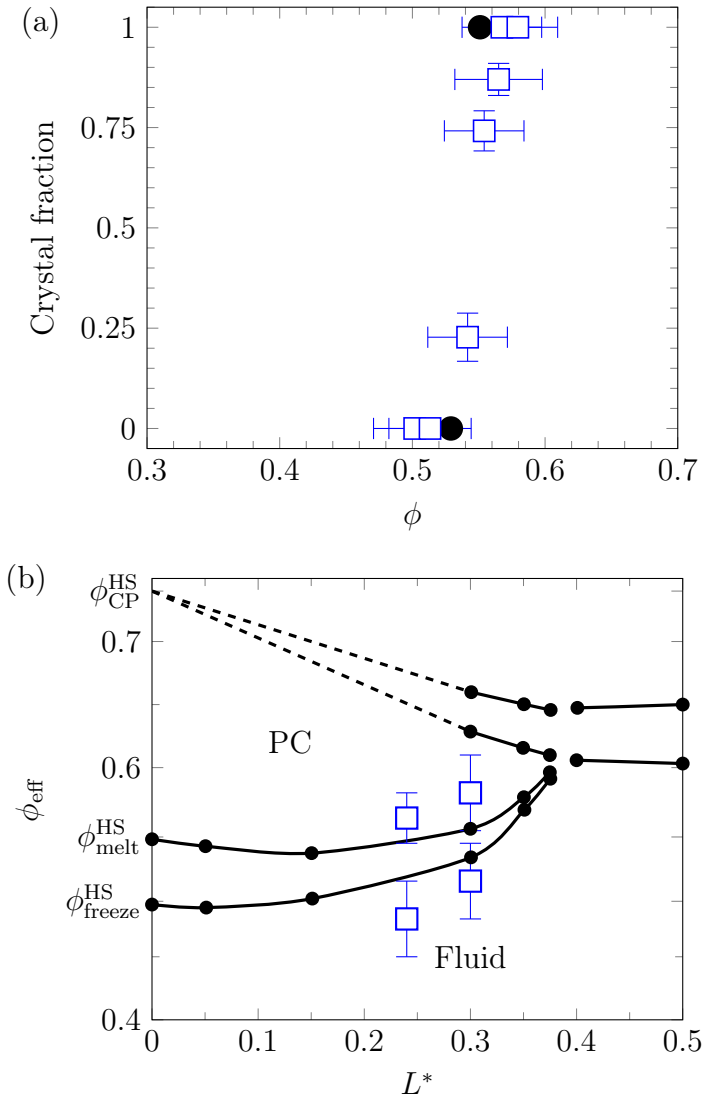

Figure 2.4: Phase equilibrium (a) of hard dumbbells at $L^* \approx 0.3$ from crystallisation experiments. The experimental coexistence points (b) (denoted by blue squares (□)) is compared with the prediction of MC simulations (solid black line (•) [77]) for $L^* = 0.24$ and $L^* = 0.30$ [119]. Adapted with permission from N. Heptner, F. Chu, Y. Lu, P. Lindner, M. Ballauff, and J. Dzubiella, Phys. Rev. E **92**, 052311 (2015) [122]. Copyright © 2015, American Physical Society.

The scattering data gathered by experimentalists may be compared to our analysis of the simulation trajectories, which allow to compute the scattering intensity $S(\mathbf{q})$ distributions according to eq. (2.33). The intensity distribution yields information on the translational and orientational structure of the probed system. This depends on the scattering geometry and the state of the probe. In crystalline samples it is strongly dependent on the orientation of the crystal with respect to the incident beam.

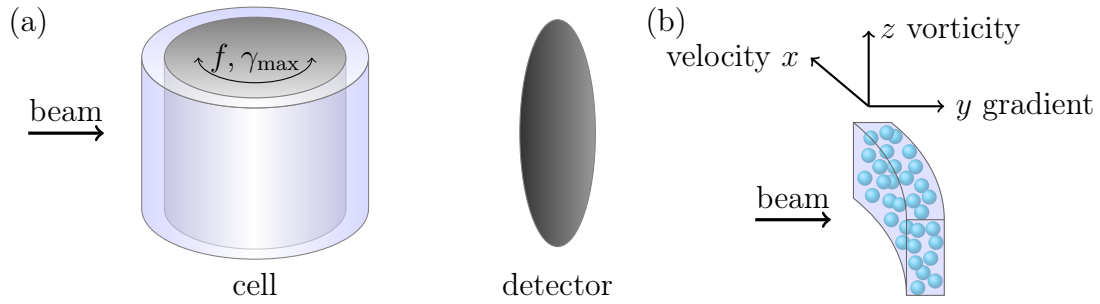

Figure 2.5: Set-up of the rheo-SANS experiment: (a) The beam is aligned with the gradient (y) direction of the flow cell, where the suspension is sheared at a fixed frequency f and strain amplitude $\gamma_{\max}$. The detector records scattering for a fixed time per strain amplitude in the velocity-vorticity ($x - z$) plane. (b) The velocity gradient is along the radial and the velocity is parallel to the tangential direction of the shear geometry.

2.3.3 Rheology

The response of a system to mechanical perturbations is subject of the field of rheology [152]. It deals with phenomena related to *fluid* and *solid* systems and states that are not fully captured in these terms. A major part is the construction of constitutive equations, which can be used in continuum mechanics to model media. The archetypical models are the viscous fluid and the linear elastic body. While in viscous case the energy of the flow dissipates into internal degrees of freedom, the ideal elastic body stores the energy analogue to Hooke's spring. In both ideal cases, the respective relevant material constants, viscosity and elasticity, are independent of the flow velocity or the magnitude of the imposed strain. Viscoelasticity is a more realistic model for many systems, which includes a combination of viscous and elastic properties. There are, though, many systems which cannot be fully described by any constitutive model, which are typically restricted to certain parameter ranges and have preconditions on the properties of the medium. In particular, this is true for systems with a complex microstructure, which certainly includes colloids.

The typical measures are the complex elastic and viscous, or equivalently, the storage and loss moduli G' and G''. Simply speaking, the modulus G' characterises the elastic response, and the G'' quantifies the viscous response. This physical analogy does not hold in the non-linear regime, so one should be careful using these terms beyond the linear viscoelastic regime. In the oscillatory shear experiment at fixed frequency f and variable strain amplitude $\gamma_{\max}$, these quantities can depend on the strain amplitude. In an experimental set-up the inner or outer cup of a

shear cell (cf. fig. 2.5a) are rotated and the stress response to the flow imposed on the system is measured. The restoring force on one of the surfaces is measured to determine the stress. In the oscillatory strain experiment at a fixed frequency f the relation [152, 153] of the stress $\sigma_{xy}(t)$ to the imposed strain amplitude can be written as

$$\sigma_{xy}(t) = \gamma_{\max} \{G'(\gamma_{\max}) \sin(2\pi f t) + G''(\gamma_{\max}) \cos(2\pi f t)\} \tag{2.64}$$

The viscoelastic response measured on plastic crystalline dumbbells with $L^* = 0.3$ at the volume fraction $\phi = 0.6$ is depicted in fig. 2.6. At rest, the elastic modulus G' exceeds the viscous modulus of the crystalline suspension by far, so one could characterise the system as solid-like. At high strain amplitudes the viscous modulus G'' dominates the system.

As displayed in Figure 2.6a, data from oscillatory rheology indicate kinetic differences as the rheology of the $L^* = 0.24$-system (cf. fig. 1.8) is retained by either the frequency or the number of shear cycles per point. The yielding behaviour displayed in Figure 2.6a shows that hard dumbbells with $L^* \approx 0.30$ in the plastic crystalline phase have one yielding event at $f = 1\,\mathrm{Hz}$ but two yielding events at $f = 5\,\mathrm{Hz}$. Compared with the oscillatory shear with $f = 1\,\mathrm{Hz}$, the number of applied shear cycles is increased by five times within the same measurement time for the oscillatory shear with $f = 5\,\mathrm{Hz}$.

Based on these three sets of experiments, it can be concluded that hard dumbbells with $L^* \approx 0.30$ in the plastic crystalline phase show the same double yielding behaviour as the hard dumbbells with $L^* \approx 0.24$, but the former needs more or faster oscillations. As discussed in fig. 2.4a, the hard dumbbells with $L^* \approx 0.30$ is closer to the glassy state than that with $L^* \approx 0.24$ at the same volume fraction of 0.6. Due to the slowdown of the dynamics in the vicinity of the glass transition, stronger and longer oscillations are required to induce the same structural evolution as that with $L^* \approx 0.24$. It is interesting to mention that the double yielding events are observed as well in the oscillatory shear field with $f = 1\,\mathrm{Hz}$ when the measurement time is extended by five times as shown in Figure 2.6b.

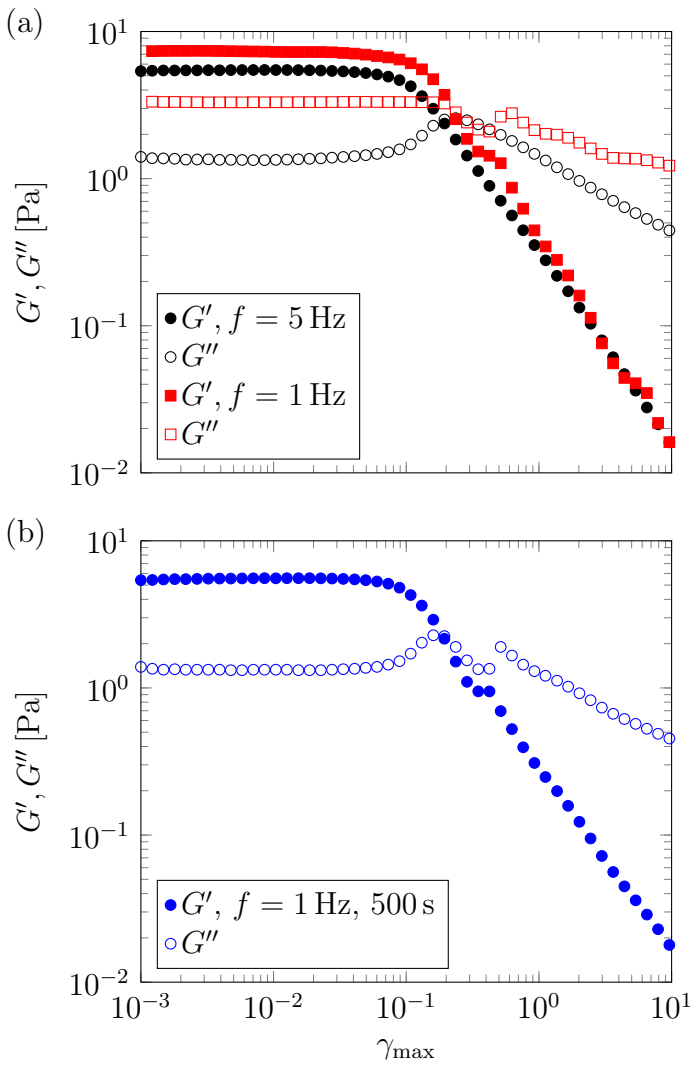

Figure 2.6: (a) Experimental dependence of G' and G'' on increasing $\gamma_{\max}$ for hard dumbbells with $L^* \approx 0.30$ in the plastic crystal phase under oscillatory shear at $f = 1\,\mathrm{Hz}$ (○●) and $f = 5\,\mathrm{Hz}$ (□■). This measurement is performed with the default setting (100 s/point). (b) Shear moduli versus strain amplitude $\gamma_{\max}$ for the same system phase that is measured under oscillatory shear of $f = 1\,\mathrm{Hz}$ with 500 s/point (○●). The filled symbols denote G', while open symbols represent G'' [119]. Adapted with permission from N. Heptner, F. Chu, Y. Lu, P. Lindner, M. Ballauff, and J. Dzubiella, Phys. Rev. E **92**, 052311 (2015) [122]. Copyright © 2015, American Physical Society.

Chapter 3

Equilibrium structure and transport properties

In this section we investigate the relation of the equilibrium structure to dynamical properties. The transport properties are calculated in the equilibrium limit in order to understand the influence of the moderate anisotropy of the dumbbell particles on these dynamic properties and their relation to the structure of the system. We first consider spatial correlations, then turn to translational and rotational relaxation properties and finally explore the zero shear limit of the viscosity.

3.1 Spatial structure

The centre of mass (COM) radial distribution functions (RDFs) of dumbbell suspensions at the volume fraction $\phi = 0.60$ are displayed for various elongations in fig. 3.1. The signature of the phase transition from plastic crystal (PC) to fluid (F) may be readily observed here. At state points with $L^* \lesssim 0.3$ the system is in the PC phase, cf. fig. 1.4, where the COM positions are frozen in a crystal lattice and the directors do not show any long-distance correlations. Hence, the corresponding RDFs show strong correlations and long-ranged oscillations. They vanish at $L^* = 0.39$, where the system is in the isotropic fluid phase.

Figure 3.1b shows the COM RDFs $g(r)$ at the fixed colloidal packing fraction $\phi = 0.44$, where all shown curves are in the F phase. With increasing elongation, the extrema get less pronounced and are shifted to greater distances due to the larger effective particle sizes.

The orientational pair correlation functions (PCFs) g_{P_2} at the volume fractions $\phi = 0.60$ and $\phi = 0.44$ are depicted in fig. 3.2 and its inset, respectively, for

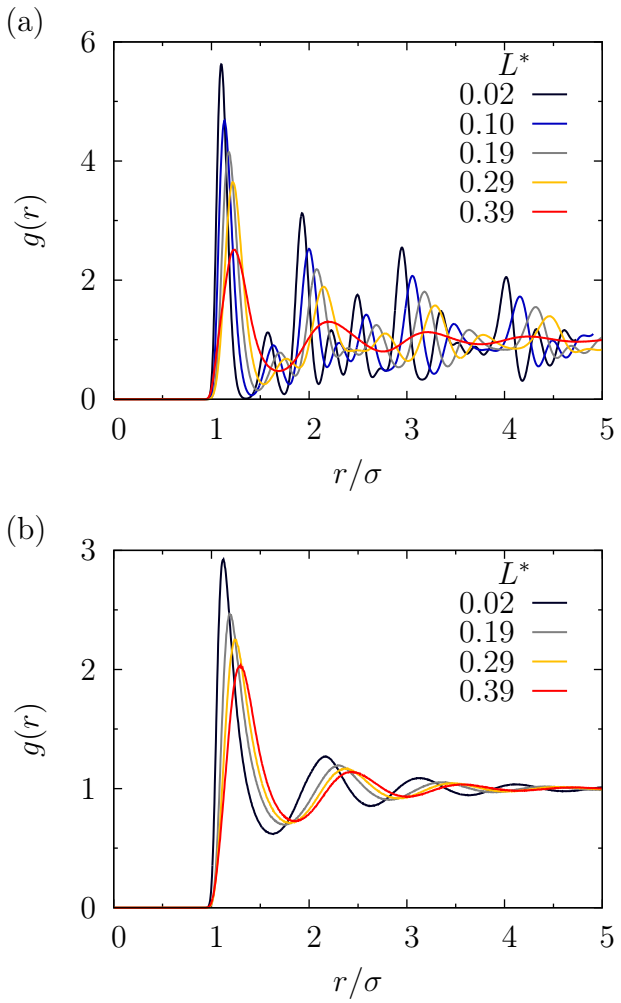

Figure 3.1: (a) The radial distribution function $g(r)$ for the dumbbell centre-of-mass at a volume fraction $\phi = 0.60$: black, blue, grey and yellow, are in the PC, and red in the F phases, respectively. (b) The same for a packing fraction $\phi = 0.44$, where all systems are in the F phase. Adapted with permission from N. Heptner, and J. Dzubiella, Mol. Phys. **113**, 2523–2530 (2015) [154]. Copyright © 2015, Taylor & Francis.

various representative elongations. As expected, the orientational correlation in space is essentially flat for suspensions of nearly spherical particles ($L^* = 0.02$) at all volume fractions. At roughly $r/\sigma \simeq 1$, the g_{P_2} for non-zero elongations show maxima indicating a strong correlation of nearest neighbours at contact. This first correlation peak moves slightly away from $r = \sigma$ as the elongation increases.

At the first maxima, the functions are positive, representing a preferably parallel orientation of dumbbell particles at close contact. For a bit larger distances, $r/\sigma \simeq 1.1 - 1.3$, negative dips indicating orientational anti-correlations are observed which tend to higher distances as the elongation is increased. These preferential

orientations are depicted in exemplary snapshots in fig. 3.3. Hence, in the F phase at $\phi = 0.60$, there are non-vanishing next-neighbour correlations which grow with elongation.

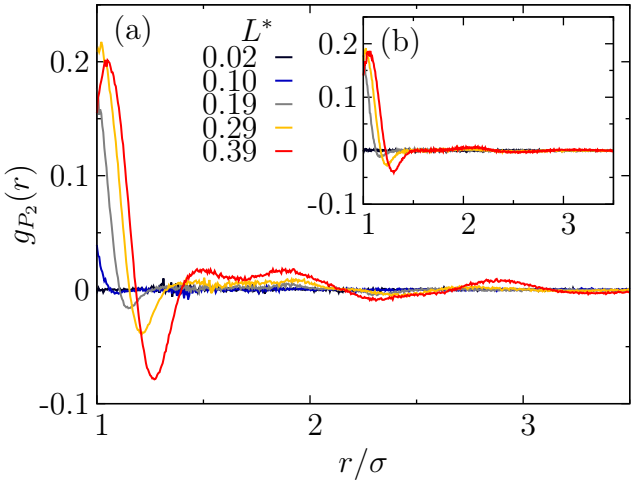

Figure 3.2: Orientational pair correlation function $g_{P_2}(r)$ at a volume fraction $\phi = 0.60$: the black, blue, and purple curves present data for the systems in the PC phase and red in the F phase, respectively. Inset: The same for a packing fraction $\phi = 0.44$ where all systems are in the F phase. Adapted with permission from N. Heptner, and J. Dzubiella, Mol. Phys. **113**, 2523–2530 (2015) [154]. Copyright © 2015, Taylor & Francis.

With further increasing aspect ratio, the orientational correlation becomes non-zero over a higher distance as the system crosses to the dense fluid phase at $\phi = 0.44$. Here, we observe a new correlation peak at in the dense fluid state for $L^* = 0.39$ close to $r/\sigma \simeq 1.8$ and 2.8, indicating growing second and third neighbour correlations. Thus, in the fluid phase the correlations are longer ranged due to the higher disorder and collisions when compared to the PC phase.

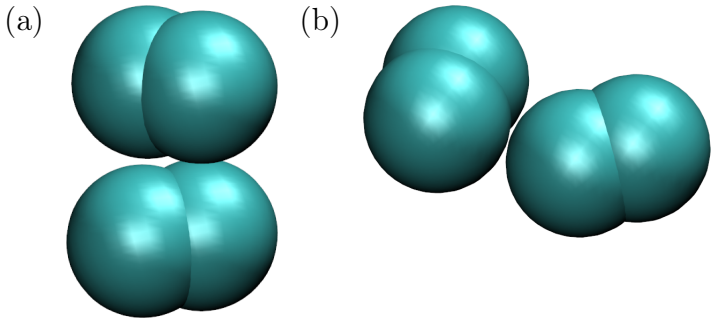

Figure 3.3: Snapshots of $L^* = 0.39$ dumbbells at $\phi = 0.6$ in close contact in nearly parallel configuration (a) and perpendicular configuration (b).

3.2 Translational diffusion

3.2.1 Time-dependent diffusion coefficient

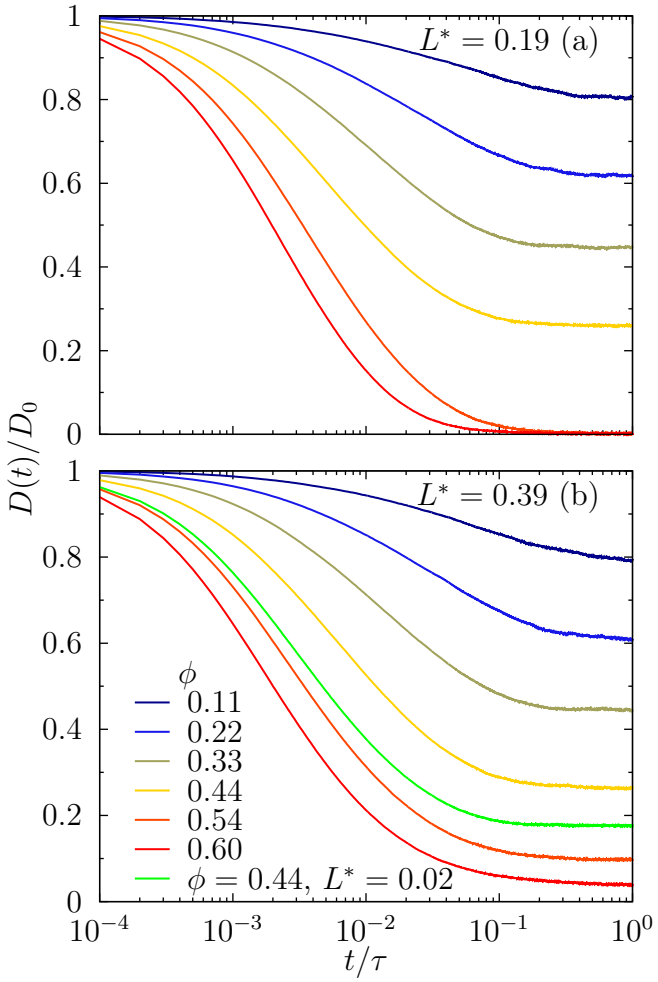

Figure 3.4: Time-dependent diffusion coefficient $D(t)/D_0$ from the velocity autocorrelation function (VACF) at (a) $L^* = 0.19$ and (b) $L^* = 0.39$ for different packing fractions. The dashed line in (b) is at state point $\phi = 0.44, L^* = 0.02$ for a direct comparison. Adapted with permission from N. Heptner, and J. Dzubiella, Mol. Phys. **113**, 2523–2530 (2015) [154]. Copyright © 2015, Taylor & Francis.

Figure 3.4a and b show the time-dependent COM diffusion coefficients $D(t)$ at constant elongation $L^* = 0.19$ and $L^* = 0.39$ for different colloidal volume fractions, respectively. At early times ($t \lesssim 10^{-4}$), before the particles feel the interacting neighbours in a non-dilute suspension, the diffusion coefficients are close to the short-time limits of a single, free particle. Within times $t \lesssim 10^{-2}\tau$, a continuous transition to long-time diffusion starts which is reached at about the Brownian time scale τ. With increasing volume fraction ϕ, the cross-over from short-time

to long-time behaviour sets in earlier and is steeper. At the elongation $L^* = 0.19$ the systems with packing fractions $\phi = 0.54$ and $\phi = 0.60$ are in the PC phase. Due to the translational constraints in the crystal, the diffusion vanishes at about a tenth of a Brownian time. The comparison of the diffusion between $L^* = 0.19$ and $L^* = 0.39$ at $\phi = 0.44$ in the dense fluid in panel (a) demonstrates that the influence of the aspect ratio is very small in the range of focus of this study. Since all the shown curves for the elongation $L^* = 0.39$ are in the F phase (panel (b)), the diffusion coefficients are not vanishing for all volume fractions.

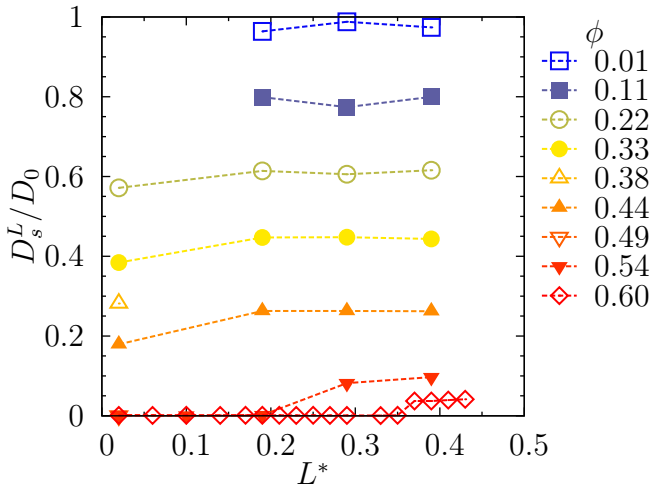

Figure 3.5: Long-time self-diffusion coefficients D_s^L obtained from the VACFs via relation (eq. (2.41)). Adapted with permission from N. Heptner, and J. Dzubiella, Mol. Phys. **113**, 2523–2530 (2015) [154]. Copyright © 2015, Taylor & Francis.

In fig. 3.5 the values of the long-time COM self-diffusion coefficients D_s^L are presented for various elongations and packing fractions. As expected, the diffusion is significantly decreased for larger packer fractions, as known for the spherical reference case. Surprisingly, the dependence of the diffusion on elongation is weak and we find that this is the case for both parallel and perpendicular long-time diffusion as well (cf. fig. 3.6). Apparently, the anisotropy is not large enough to substantially change the long-time (single colloid) friction in these systems. Furthermore, the data shows a discontinuous transition to vanishing diffusion at elongations where the transition to the PC phase takes place, see the curves for the large packing fractions $\phi \geq 0.54$.

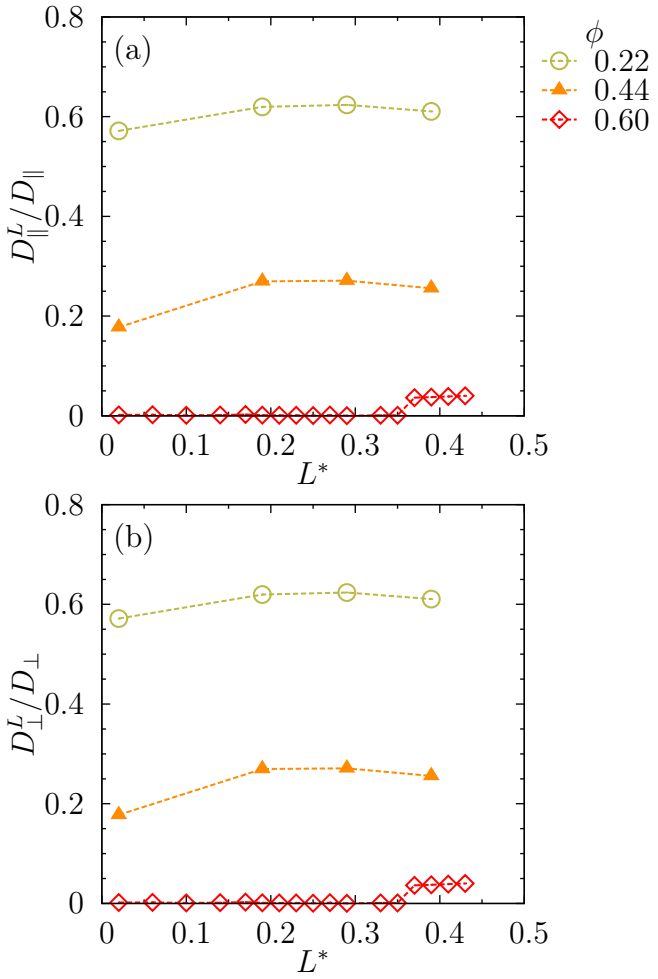

Figure 3.6: Parallel $D_\parallel^L$ (a) and perpendicular $D_\perp^L$ (b) long-time diffusion coefficients obtained according to eq. (2.52) at exemplary volume fractions in the fluid ($\phi = 0.22$), very dense fluid ($\phi = 0.44$) and PC ($\phi = 0.60$).

3.3 Rotational relaxation and diffusion

Figure 3.7 shows the rotational diffusion coefficients obtained from exponential fits to the directional autocorrelation functions (DACFs). At small elongations $L^* \lesssim 0.2$ the rotational diffusion is almost constant with respect to volume fraction, albeit the system crosses from the F to the PC phase at high fractions. Hence, for these small elongations the particles indeed rotate almost freely in the PC phase. The obvious statistical outliers in the rotational diffusion data for small packing fractions $\phi \lesssim 0.3$ are within the statistical error of $\pm 5\%$, estimated from block averages over independent trajectories of length of 10τ. However, suspensions of dumbbells with $L^* = 0.29$ show a notable drop of the rotational diffusion coefficients for densities higher than $\phi = 0.5$ and packing effects clearly influence the rotation correlations in the PC phase. On increasing the elongation further, now a clear non-linear

density-dependence of the rotational relaxation emerges which becomes obvious for $L^* = 0.39$ for packings larger than $\phi \gtrsim 0.3$. Here, the system is in the fluid phase only and the closer contacts in the disordered systems alter the rotational dynamics substantially. At the highest investigated packing fraction ($\phi = 0.60$) the rotational diffusion drops down by more than 30 %.

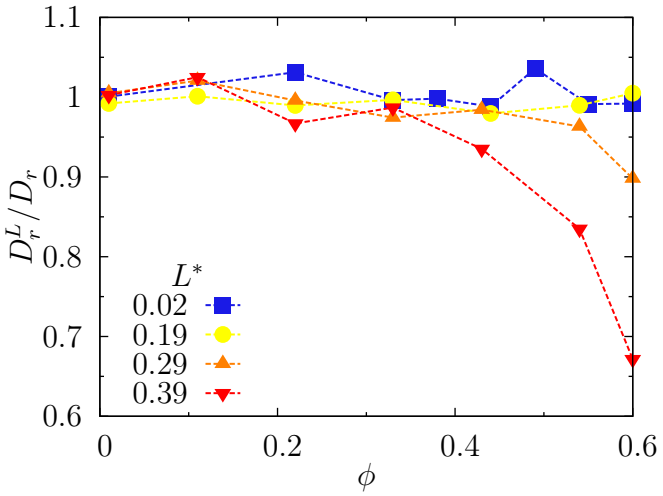

Figure 3.7: Dependence of rotational diffusion coefficients D_r^L at various elongations from exponential fits to DACF on volume fraction ϕ. The statistical error of the data is estimated from the variation of the variation of exemplary identical systems to be about 5 %. Adapted with permission from N. Heptner, and J. Dzubiella, Mol. Phys. **113**, 2523–2530 (2015) [154]. Copyright © 2015, Taylor & Francis.

3.4 Shear viscosity

Figure 3.8 shows the stress autocorrelation functions (SACFs) at various aspect ratios L^*. For the smaller packing fractions $\phi < 0.5$, the correlation functions decay slower for higher densities while the elongation dependence is rather weak. However, at the volume fraction $\phi = 0.60$ the system is in the PC phase for the shown elongations, except for $L^* = 0.39$. Here an interesting behaviour can be observed: at $L^* = 0.02$ the SACF decays more rapidly in the PC state point than in the fluid states. However, for the next two larger elongations $L^* = 0.19$ and $L^* = 0.29$, the SACF decays slower and develops a new slow time scale for times about $10^{-1}\tau$ in the PC phase. This must be assigned to slow stress relaxations in the dense crystal phase likely stemming from more pronounced translational-rotational couplings [73], since they are absent for the small elongations at the same density. This long-time tail occurring in the PC phase seems to diminish when crossing into the F phase by

increasing the aspect ratio to $L^* = 0.39$.

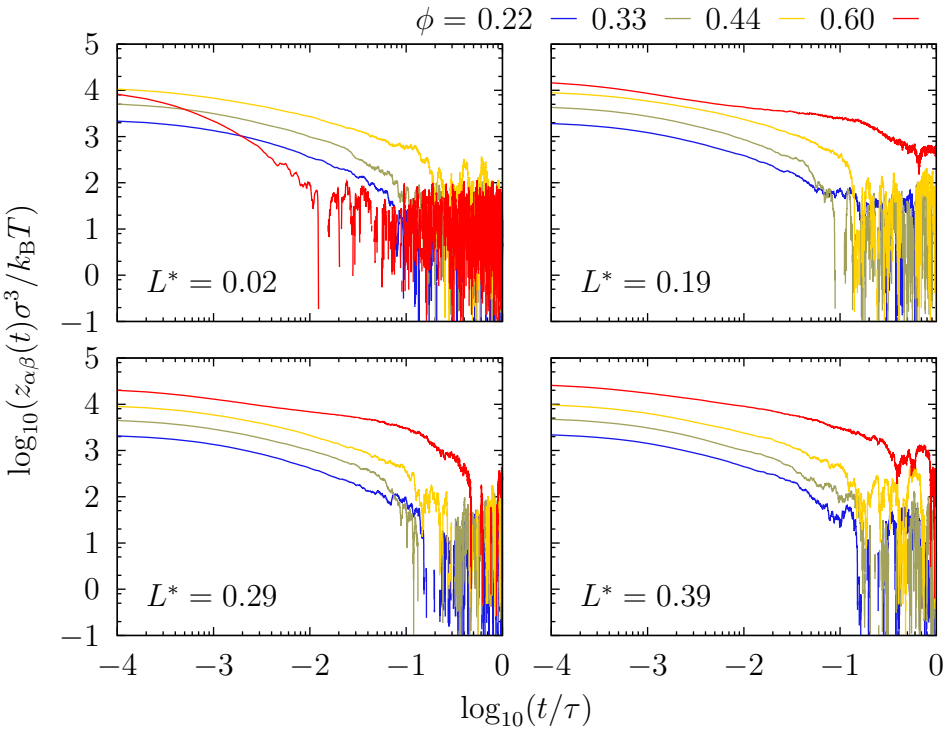

Figure 3.8: SACFs at different elongations (increasing from top left to bottom right panels) and volume fractions each. Notably, the nearly spherical system shows a rapid decay in the PC phase. Adapted with permission from N. Heptner, and J. Dzubiella, Mol. Phys. **113**, 2523–2530 (2015) [154]. Copyright © 2015, Taylor & Francis.

Figure 3.9a shows the packing fraction dependence of the relative steady shear viscosity $\eta_{r0} = \eta_0/\eta_s$ for different elongations L^*, with η_s being the viscosity of the suspending medium. These data are obtained from integration of the SACFs in fig. 3.8. As an important comparison, also the hard sphere (HS) reference data following the empirical Krieger-Dougherty relation [130, 133] for the *purely fluid* phase is shown. As we readily see, there is a difference of the viscosity for a fluid of HSs when compared to our minimal elongation data (at $L^* = 0.02$). This can be understood as a result of the sensitivity of viscosities to the softness of the chosen pair potential for repulsive spheres [131]. In the present case, the $L^* = 0.02$ system with minute anisotropy can be considered equal to the purely spherical system. At higher packing the HS system is in the crystal phase and the linear shear response drops to zero (and not accounted for in the fluid-state Krieger-Dougherty approach). The shear viscosity of dumbbells is similar to the HS system in the fluid phase below packings of $\phi \lesssim 0.45$ but deviates strongly for larger packings for all elongations

where the dumbbell shear response substantially increases with L^*. We explain the increase by the long time tails in the SACFs in fig. 3.8 due to the relaxation of the rotational degrees of freedom missing in the HS case. The large increase of the shear response is somewhat unexpected since the translational degrees of freedom are still frozen, except for the largest elongation $L^* = 0.39$ for which all shown data are in the fluid phase. We note that the error bars of this data are hard to estimate due to the long-time tails in the SACFs. While we believe from the systematic behaviour of the data that the trends are reliable, small fluctuations of the data as for $\phi = 0.44$ are very probable within the statistical uncertainty.

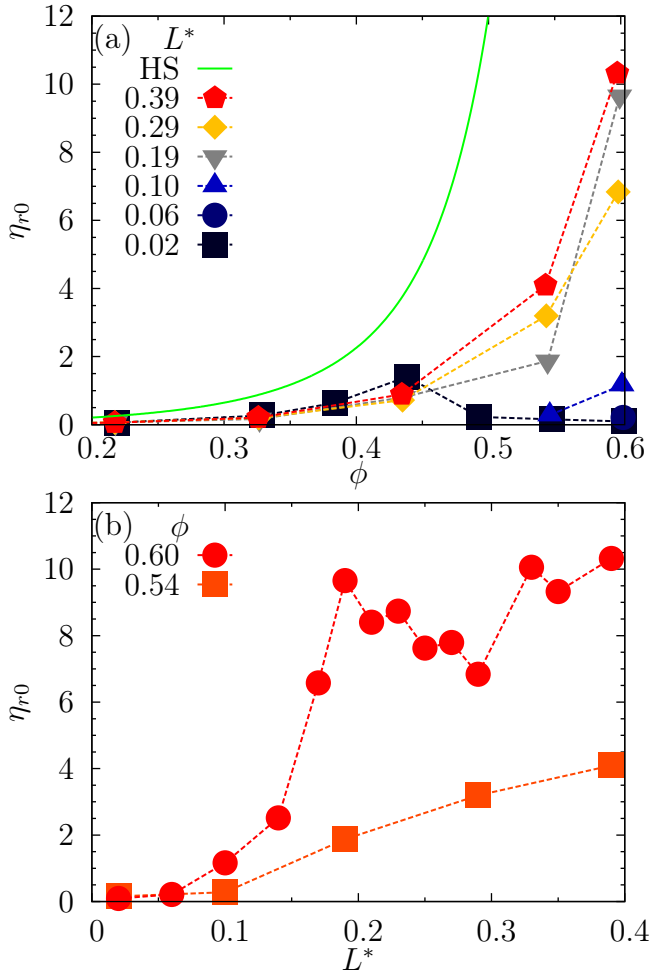

Figure 3.9: Steady shear relative viscosity difference η_{r0} (a) as a function of the volume fraction ϕ and (b) versus elongation L^* at high densities. The HS line (–) refers to the phenomenological Krieger-Dougherty theory [130, 133]. Adapted with permission from N. Heptner, and J. Dzubiella, Mol. Phys. **113**, 2523–2530 (2015) [154]. Copyright © 2015, Taylor & Francis.

Figure 3.9b shows the dependence of the relative steady shear viscosity on the elongation at the high packing fractions $\phi \geq 0.39$. This view reveals a transition

from the hard spherical case of almost vanishing viscosity to a finite level at about a critical elongation of about $L^* = 0.15$. This is most evident at the highest packing fraction where the transition is relatively steep. (The fluctuations of the data between $L^* = 0.2$ and 0.3 is most certainly due to the statistical uncertainty.) Hence, it may be inferred from the equilibrium linear response data that a small deviation from the spherical shape already to an aspect ratio of $L^* \gtrsim 0.15$ induces a dramatic collective response that manifests itself in a large increase of the linear response shear viscosity.

3.5 Summary

In summary, we have investigated the equilibrium structure and fluctuations of colloidal dumbbells by means of Brownian Dynamics computer simulations. We focused on high packing fractions and on the weak elongation regime ($L^* < 0.4$) where the dumbbells are predominantly in the plastic crystal phase. Our systematic investigation revealed the expected structural changes with larger elongation with respect to the hard sphere reference case and very localised orientational correlations, typically just involving next-neighbour correlations. These relatively weak correlations are also reflected in only minor changes in the translational and rotational diffusion coefficients for most of the investigated elongations, except for the highest elongation in the fluid phase where the rotational diffusion drops by ca. 30 % when compared to the free rotation. However, the linear response shear viscosity exhibits a dramatic increase even in the plastic crystal phase at high packing fractions ($\phi \gtrsim 0.5$) beyond a critical elongation of about $L^* = 0.15$. This result is surprising in view of the relatively weak effects of elongation found before. Here one should rationalise that the linear response shear viscosity expresses collective relaxation time scales and not (more local) single molecule dynamic properties. Apparently beyond a critical, surprisingly small anisotropy, newly occurring rotational-translational couplings must be made responsible for the slow time scales appearing at higher elongations in the crystal [73]. Hence, more detailed calculations and modelling of these rotational-translational correlations in weakly anisotropic model systems shall be interesting for future studies, in particular beyond linear response where probably more substantial dynamical effects of increased anisotropy may occur [115].

Chapter 4

Hard dumbbells under oscillatory shear

In this section we turn to the structure of hard dumbbells under shear conditions. While the work on linear response dynamical properties is restricted to vanishing external fields, the following research is explicitly focused on the effect of oscillatory shear on the structure of dumbbell suspensions. The external driving is beyond the linear limit, where the systems exhibit steady non-equilibrium states. Here we restrict our interest to dumbbell suspensions in the plastic crystal (PC) equilibrium phase at high densities and elongations below $L^* \leq 0.4$. For the readers' orientation, the investigated state points in the volume fraction ϕ and elongation L^* are indicated in fig. 4.1.

Let us start with some striking experimental observations for dumbbells with $L^* = 0.24$. First, from the rheo-small-angle neutron scattering (SANS) we learn about the structure of the samples at the specific imposed strain amplitudes. This is compared to the scattering intensities $I(\mathbf{q})$ calculated according to eq. (2.33) from the non-equilibrium Brownian dynamics (NEBD) trajectories in fig. 4.2. Here, the row (a) depicts intensity patterns in the velocity-vorticity ($x - z$) plane and the column (b) shows the corresponding patterns obtained in the rheo-SANS experiment in the states I, II and III [115, 119]. These states are defined by their respective structural properties and the transitions between these states have a vigorous impact on the non-linear rheology (cf. figs. 1.8 and 2.6). The rheological experiments have been conducted under sinusoidal oscillatory shear with increasing amplitudes [115, 119] and scattering data has been recorded at each imposed amplitude (cf. section 2.3.2). This structural transition is accompanied by a two-step yielding event upon increasing strain amplitudes in the large amplitude oscillatory shear experiment (cf. figs. 1.8 and 2.6), which motivates this investigation

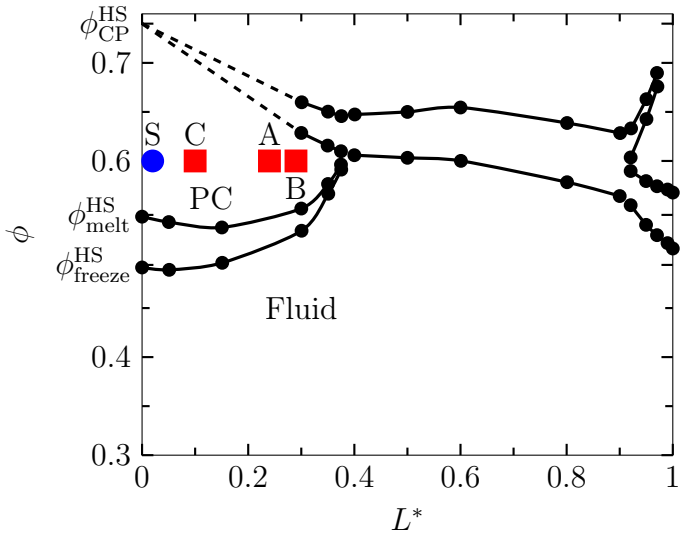

Figure 4.1: Hard dumbbell phase diagram in the volume fraction ϕ to aspect ratio L^* plane [77]. The state points for dumbbells A ($\phi = 0.60$, $L^* = 0.24$), B ($\phi = 0.60$, $L^* = 0.29$), and C ($\phi = 0.60$, $L^* = 0.1$), considered in this work are marked by symbols (red squares). The blue symbol (state point S) depicts an almost hard-sphere-like reference system ($\phi = 0.60$, $L^* = 0.02$). For better orientation, the freezing, melting and close packed packing densities of the hard sphere (HS) system are indicated at the vertical axis. Adapted with permission from N. Heptner, F. Chu, Y. Lu, P. Lindner, M. Ballauff, and J. Dzubiella, Phys. Rev. E **92**, 052311 (2015) [122]. Copyright © 2015, American Physical Society.

of the structural origins. The colloidal nitrogen system ($L^* \approx 0.3$, state point B) shows the same states on increasing strain amplitude as system A, both in the present simulations and the rheo-SANS experiments (fig. 2.6). The main difference is that the longer dumbbells needs larger Péclet numbers Pe_r to induce the same non-equilibrium phase as compared with hard dumbbells with $L^* \approx 0.24$. Thus, the data from oscillatory rheology indicate kinetic differences, because the rheology of the system A is retained by either the frequency or the number of shear cycles per point.

Our NEBD simulations are conducted using the same protocol, with concessions for feasibility in the computational time. On the one hand, we neglect hydrodynamic interactions, which is justified in the range of our external driving. On the other hand, we accept differences in the time scales due to this neglect. It should be noted that the simulations are carried out at a higher shear frequency. In the steady state, though, these differences should not be dominant, such that our simulations may reasonably be compared to these experiments.

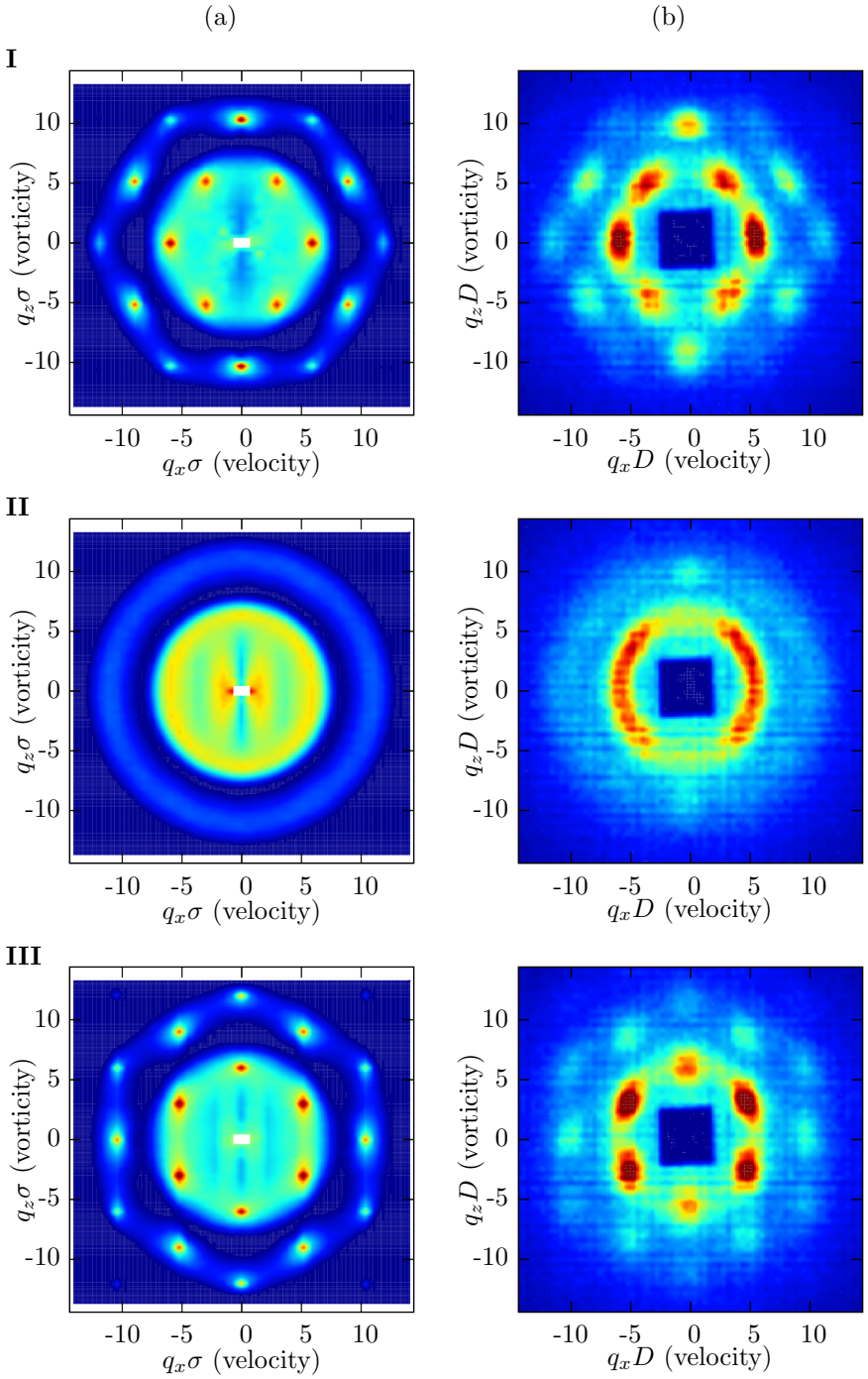

Figure 4.2: Scattering intensity patterns of states I, II and III from a) NEBD simulations at $f = 5/\tau$ and b) rheo-SANS experiments at $f = 1\,\mathrm{Hz}$ for system A. Experimental data replotted from references [115, 119]. The exemplary intensity distributions have been chosen at the strain amplitudes $\gamma_{\max} = 0.15$, $\gamma_{\max} = 0.5$ (I); $\gamma_{\max} = 0.2$, $\gamma_{\max} = 0.6$ (II) and $\gamma_{\max} = 0.3$, $\gamma_{\max} = 1.16$ (III) in simulations and experiments respectively. Adapted with permission from F. Chu, N. Heptner, Y. Lu, M. Siebenbürger, P. Lindner, J. Dzubiella, and M. Ballauff, Langmuir **31**, 5992–6000 (2015) [115]. Copyright © 2015, American Physical Society.

4.1 Structure upon increasing shear strains

We start with the discussion of simulated scattering intensities for selected state points. In fig. 4.3 the scattering intensities $I(\mathbf{q})$ including the scattering amplitude calculated as defined in equations eq. (2.33) and eq. (2.34) are shown in the velocity-vorticity plane. The data corresponds to state point B, cf. fig. 4.1, at a frequency of $5\tau^{-1}$ for selected strains. A common feature of the intensity plots is the fact that the maxima are located on rings of constant magnitude of the scattering vector. The intensity plots illustrate the transition from the low strain twinned crystal state (I) to the high strain sliding layer state (III), corroborating with above results on a smaller aspect ratio [115]. In the fully ordered states, the systems tend to form two-dimensional hexagonal close packed (hcp) layers in the velocity-vorticity $(x - z)$ plane, which is indicated by the hexagonal symmetry of the peaks in the intensity patterns. These planes are the most densely packed crystallographic planes for face-centered cubic (fcc) and hcp crystal structures and their stacking sequence determines the crystallographic type. In the experiments, the systems are polycrystalline at rest and the crystallites are oriented due to the shear at an amplitude of about $\gamma_{\max} \approx 0.2$ [115, 119].

At low strain amplitudes (fig. 4.3a,b) a shear-twinned fcc crystal is stable, which has a densely packed direction perpendicular to the velocity direction, while at high strains (fig. 4.3d-f) a dense direction parallel to the velocity is favourable. Similar transitions had been observed in spherical systems [100, 102, 103]. However, slightly anisotropic dumbbells introduce an additional orientational degree of freedom, and, although weak, it leads to a more abrupt transition compared to the spherical case [115]. In equilibrium terms it could be said that the mild anisotropy qualitatively change the transition from being continuous to discontinuous. This phenomenon is already present in the series of scattering intensities, as we observe a fully molten intermediate state, cf. fig. 4.3c. In contrast, for the hard spherical reference case, we always detect order in form of crystalline hybrids exemplary depicted in fig. 4.8c. At a strain amplitude about $\gamma_{\max} \approx 0.2$ the system does not show long-range correlation and is nearly isotropic (fig. 4.3c). Close to this transition an anisotropy at very small scattering vectors can be observed in the reciprocal velocity-vorticity plane. Above this isotropic state II, hexagonal layers are formed (state III), which are oriented with their densest direction along the velocity direction. This is clearly indicated by a 30 ° tilt of the scattering pattern compared to the state I. From comparison to the idealised picture given by Loose and Ackerson [103] and from the reasoning concerning the volume fractions given by Ackerson [111] one learns

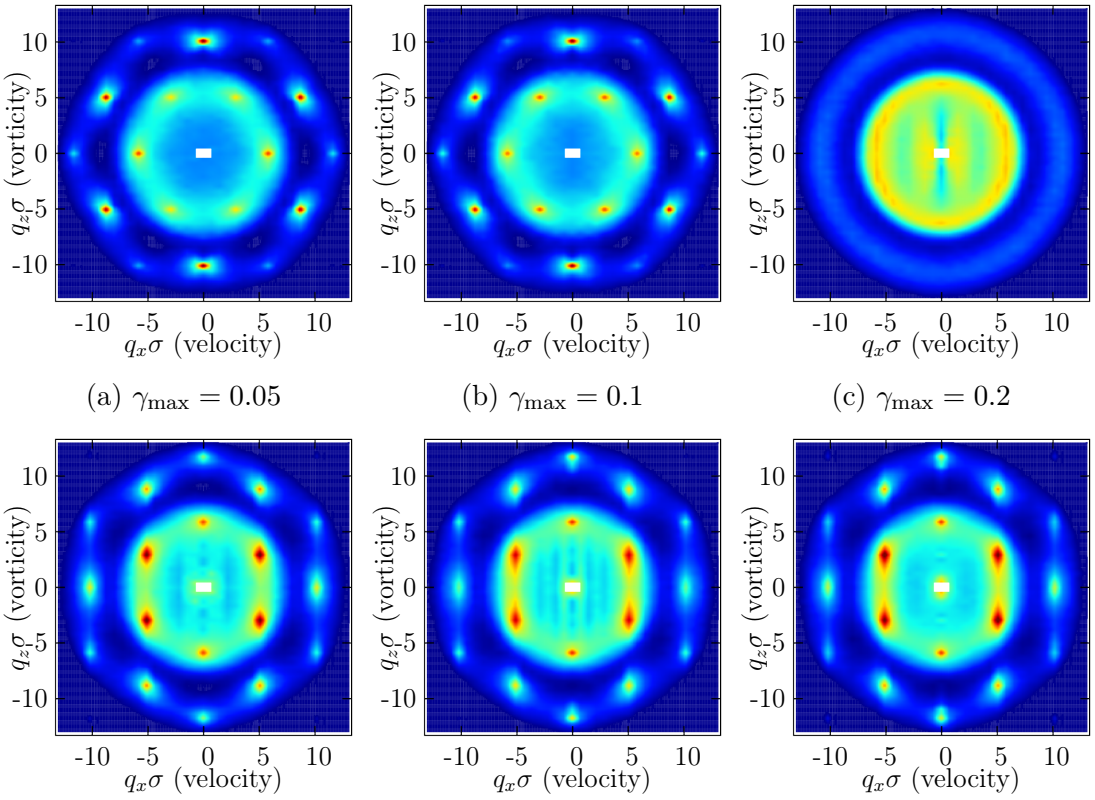

(a) $\gamma_{\max} = 0.05$ (b) $\gamma_{\max} = 0.1$ (c) $\gamma_{\max} = 0.2$

(d) $\gamma_{\max} = 0.3$ (e) $\gamma_{\max} = 0.5$ (f) $\gamma_{\max} = 1.0$

Figure 4.3: Scattering intensities $I(\mathbf{q})$ (250 cycles averaged) in the $q_y = 0$ plane of sheared dumbbell suspensions ($L^* = 0.29, \phi = 0.60$, state point B) at frequency $f = 5\tau^{-1}$. From top left to bottom right: increasing strain amplitude $\gamma_{\max}$. Adapted with permission from N. Heptner, F. Chu, Y. Lu, P. Lindner, M. Ballauff, and J. Dzubiella, Phys. Rev. E **92**, 052311 (2015) [122]. Copyright © 2015, American Physical Society.

that the centre of mass (COM) motion of the dumbbells follow strongly registered zig-zag trajectories while maintaining two-dimensional hexagonal in-plane order. In the literature, two different modes of motion allowing to sustain ordered layers at high strain amplitudes have been identified [102, 103]. The straight sliding of neighbouring layers past each other has been linked to vanishing inner peaks [103] on the vorticity axis ($q_x\sigma = 0$), which clearly is not the case for systems A and B (cf. fig. 4.2III and fig. 4.3d-f).

In the following, we quantify the particles' orientational and translational structure under the action of shear quantified by order parameters. Figure 4.4 summarises the structural information in terms of averaged order parameters for state points A and B, cf. fig. 4.1, at a frequency of $5\tau^{-1}$. Figure 4.4a shows that the average $\langle P_2^x \rangle$, quantifying the average dumbbell orientation along the flow

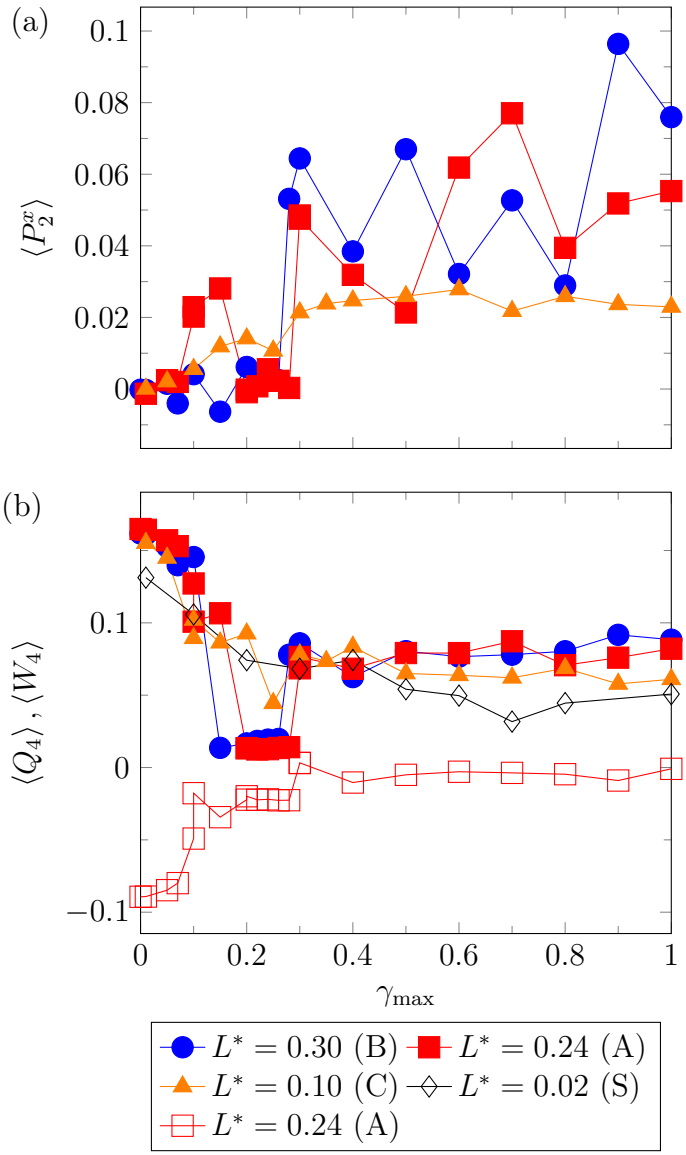

Figure 4.4: Order parameters for state points at $f = 5\tau^{-1}$. (a) Averaged orientational order parameter in flow direction $\langle P_2^x \rangle$, and (b) translational order characterised by $\langle Q_4 \rangle$ (filled symbols) and $\langle W_4 \rangle$ (open squares). Adapted with permission from N. Heptner, F. Chu, Y. Lu, P. Lindner, M. Ballauff, and J. Dzubiella, Phys. Rev. E **92**, 052311 (2015) [122]. Copyright © 2015, American Physical Society.

direction, is slightly increasing with strain for both aspect ratios in the fcc state until it drops to zero in the disordered state and is non-zero again in the high-strain regime. In fig. 4.4b the translational order, described by $\langle Q_4 \rangle$, is shown for the dumbbells compared to the nearly hard sphere reference case (S). The behaviour at the transition shows clearly that the orientational and translational order changes abruptly in a discontinuous fashion for dumbbells, while, in contrast, the transition

in suspension of hard *spheres* has a continuous character. This behaviour is retained for dumbbells with a slender elongation of $L^* = 0.10$ (system C), which show an ordered state at all investigated strain amplitudes. The average $\langle P_2^x \rangle$ for state point C shows a slight increase at low strain amplitudes as well approaching a plateau value of about 0.02 in a continuous fashion beyond $\gamma_{\max} \gtrsim 0.3$. This corresponds well to our previous finding (cf. section 3.4) that long-time stress correlations become important for dumbbells above approximately $L^* = 0.15$ [154]. Additionally, the negative $\langle W_4 \rangle$ in state I indicates fcc dominated structure, in state III this parameter vanishes on average indicating loss of fcc order.

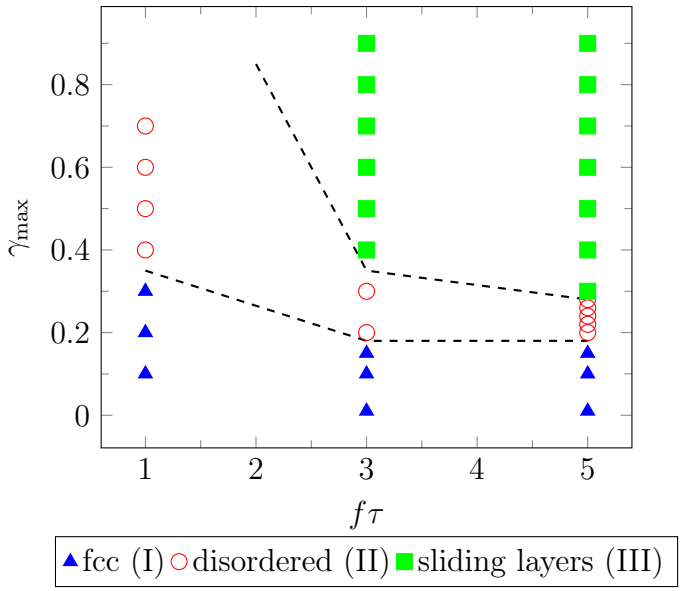

Figure 4.5: Out-of-equilibrium states [I: twinned fcc (blue triangles), II: disordered (red circles), III: sliding layers (green squares)] observed in the frequency-strain ($f\tau$-$\gamma_{\max}$) plane of the parameter space in our NEBD simulations at state point A, cf. fig. 4.1. The dashed lines are tentative boundaries of the respective non-equilibrium states. Adapted with permission from N. Heptner, F. Chu, Y. Lu, P. Lindner, M. Ballauff, and J. Dzubiella, Phys. Rev. E **92**, 052311 (2015) [122]. Copyright © 2015, American Physical Society.

Moreover, the steady states depend on the shear frequency, which is summarised in fig. 4.5. Here, we show the strain amplitude $\gamma_{\max}$ and frequency f state diagram for state point A. In our simulations, state III does not appear at $f = 1/\tau$ whereas state I is stable up to $\gamma_{\max} \approx 0.30$. For higher frequencies $f = 3/\tau$ and $f = 5/\tau$ we observe the ordered state III above an amplitude of approximately 0.3, moving slightly to lower strains on increasing frequencies, which is sketched by the dashed lines in fig. 4.5. In the NEBD simulations at constant frequency ($f = 5\tau^{-1}$) (fig. 4.4)

we observe the transition for systems A and B at nearly the same strain amplitude, while for both cases this transition clearly occurs at lower amplitudes.

4.1.1 Twinned-fcc regime (I)

Let us characterise the respective non-equilibrium states in more detail. At low strain amplitudes a shear-twinned fcc dominated structure is observed in the steady state. Figure 4.6 shows a series of snapshots taken at distinctive points in the strain cycle at which the instantaneous strain is minimal ($\gamma(t) = -\gamma_{\max}$), zero ($\gamma(t) = 0$) or maximal respectively.

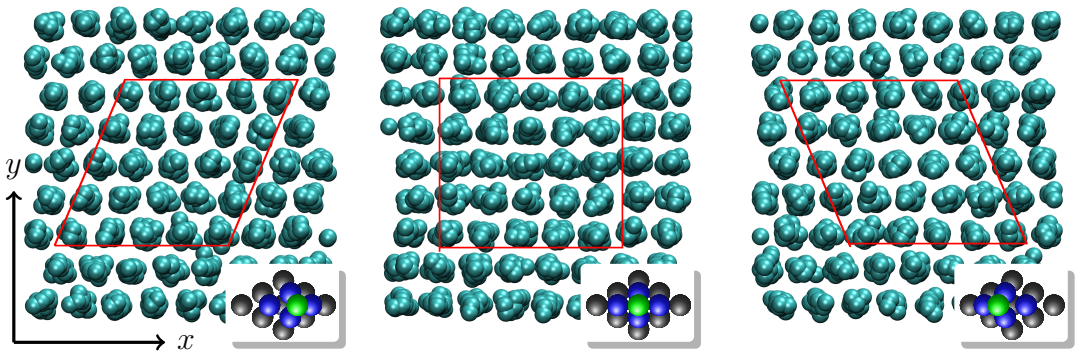

(a) maximum (b) zero (c) minimum

Figure 4.6: Simulation snapshots at prominent points in the shear cycle for $\gamma_{\max} = 0.3, f = 1\tau^{-1}$ for state point A in the twinned fcc state I at (a) maximum, (b) zero, and (c) minimum instantaneous strain in the shear cycle. The particle radii are scaled by 1/2. The insets show the models for the $x-z$-plane developed by [100, 102]. Adapted with permission from N. Heptner, F. Chu, Y. Lu, P. Lindner, M. Ballauff, and J. Dzubiella, Phys. Rev. E **92**, 052311 (2015) [122]. Copyright © 2015, American Physical Society.

In this state, particles may follow the oscillatory flow and transfer between the triangular voids offered by neighbouring layers. These void spaces are accessible in the vicinity of the extrema of the strain cycle (cf.fig. 4.6a and c), in between the particles are forced to pass particles of adjacent layers closely, which is referred to as bridge-stacking (cf. fig. 4.6b). This behaviour finds expression in the transient orientation which is subtly coupled to the strain cycle through particle interaction. At these low strain amplitudes, $\gamma_{\max} < 0.1$, the orientation shows a interplay between the velocity and the vorticity axes while the amplitude in both is very small. This is exemplified in fig. 4.7a, where we show the time-resolved orientation in one shear cycle. In approaching the transition to the high strain state, $0.1 \leq \gamma_{\max} \leq 0.2$,

the amplitudes of the $\langle P_2^x \rangle_{\text{cycle}}$ and $\langle P_2^z \rangle_{\text{cycle}}$ are still in the order of the average. The shear twinned fcc has a signature in the structure factor, see fig. 4.3a,b: the inner peaks are forbidden for equilibrium fcc crystals, in the present case we clearly observe non-vanishing peaks on the first ring and we see that their magnitude grows on increasing strain. Additionally, let it be noted, that the peaks on the velocity axis ($q_z = 0$) are the first to rise at very low strain amplitudes.

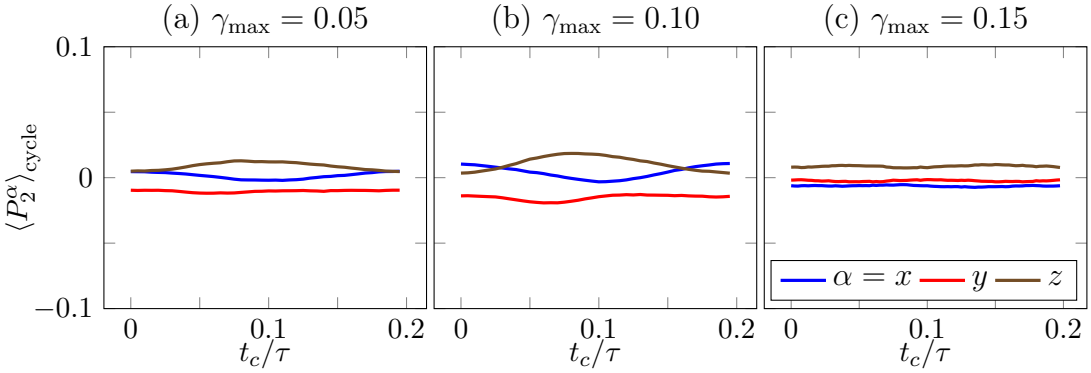

Figure 4.7: Time-resolved orientation within one cycle (averaged over 250 cycles) at frequency $f = 5\tau^{-1}$, elongation $L^* = 0.29$ (state point B), volume fraction $\phi = 0.60$, and for different strain amplitudes: (a) $\gamma_{\max} = 0.05$, (b) $\gamma_{\max} = 0.10$, and (c) $\gamma_{\max} = 0.15$. Adapted with permission from N. Heptner, F. Chu, Y. Lu, P. Lindner, M. Ballauff, and J. Dzubiella, Phys. Rev. E **92**, 052311 (2015) [122]. Copyright © 2015, American Physical Society.

4.1.2 Intermediate disordered state (II)

While for suspensions of hard spheres a disordered state in between the low-strain twinned-fcc (I) and high-strain sliding layer (III) regimes is not observed, in fact, we find stable hybrid structures on reduction of the anisotropy (cf. fig. 4.9), for sufficiently elongated dumbbells the low-strain structure always melts fully at intermediate strain amplitudes.

We neither find long-ranged translational order nor any orientational correlations whatsoever, which is confirmed considering the scattering intensities in fig. 4.3c. A representative snapshot and cycle-averaged orientations are shown in fig. 4.8, clearly demonstrating disorder. Evidently, this is a distinctive behaviour introduced by the orientational degree of freedom of the particles with a sufficient elongation. This finding is corroborating with rheo-SANS experiments, where a coexistence of states I, II and III is observed (cf. fig. 4.2IIb), the NEBD results show a fully molten

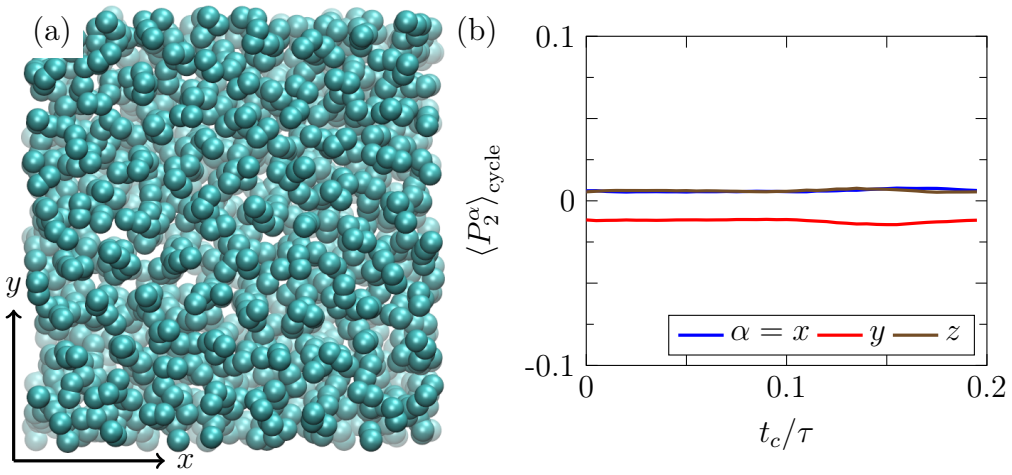

Figure 4.8: System B in the fully disordered state II at $\gamma_{\max} = 0.2$, snapshot (a), cycle averaged orientational order parameters $\langle P_2^\alpha \rangle_{\text{cycle}}(t_c)$ (b). Adapted with permission from N. Heptner, F. Chu, Y. Lu, P. Lindner, M. Ballauff, and J. Dzubiella, Phys. Rev. E **92**, 052311 (2015) [122]. Copyright © 2015, American Physical Society.

state. The limited extent of the simulated system is most probably impeding a coexistence of different crystallites and fluid.

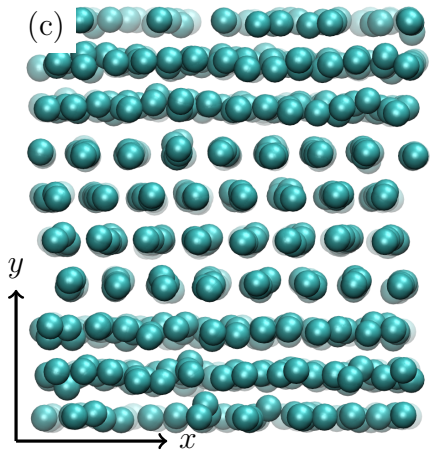

Figure 4.9: Nearly spherical reference system (S) at intermediate strain amplitude ($\gamma_{\max} = 0.50$) showing a stable hybrid crystal-like structure where a twinned fcc is in coexistence with the sliding layer phase (c).

In contrast to the melt of elongated particles, we observe stable hybrids of velocity- and vorticity-oriented spherical particles as depicted in fig. 4.9. Here, the inner layers in the simulation box sustain the twinned fcc state, while some outer layers are sliding in a velocity-oriented manner.

4.1.3 Sliding layer regime (III)

As stated above, one can conclude from the scattering patterns that the centres of masses perform a zig-zag motion while frozen in ordered hcp layers. From the order parameter study in fig. 4.4 a tendency of the particles' orientation towards the velocity axis (x) is observed, directly after reaching the critical strain to assemble into velocity oriented layers.

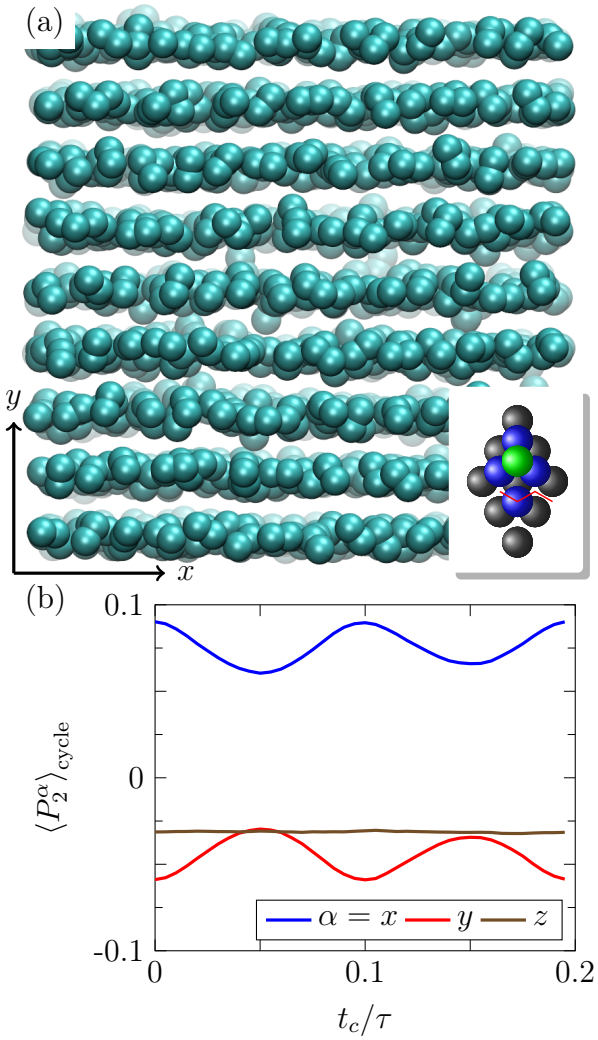

Figure 4.10: Snapshot in the flow-gradient ($x-y$) plane with model as inset (a) and oriental order parameters (b) in velocity (x), gradient (y) and vorticity (z) directions versus strain cycle at $\gamma_{\text{max}} = 1.00$ for state point B. The inset shows the model by [100, 102]. Adapted with permission from N. Heptner, F. Chu, Y. Lu, P. Lindner, M. Ballauff, and J. Dzubiella, Phys. Rev. E **92**, 052311 (2015) [122]. Copyright © 2015, American Physical Society.

Figure 4.10 shows the cycle averaged orientation in the high strain regime,

where a dense direction of each layer is aligned with the velocity direction. Here, the velocity (x) and gradient (y) directions of the directors are on average clearly modulated by the shear cycle, while the vorticity (z) direction is essentially flat. In this case, the modulus of the P_2^x cycle average is maximal at times, when the instantaneous strain vanishes ($\gamma(t) = 0$), and its amplitude is about 0.01 and its average 0.06. On average the directors slightly tend to be parallel to the velocity and perpendicular to the gradient. This coincides with a decoupling of the orientation from the imposed strain $\gamma(t)$, where the amplitudes of the $\langle P_2^\alpha \rangle_{\text{cycle}}$ are significantly smaller than their respective averages. The non-vanishing finite preferential orientation is leading to the conclusion that the high strain state is a new partially oriented sliding layer state only observed in systems of finite anisotropy.

4.2 Kinetic properties

Let us now turn our focus to rotational relaxation properties and particle collision rates. Figure 4.11a shows the inverse relaxation constant τ_r^{-1} obtained from the exponential decays of the orientational autocorrelation functions according to eq. (2.55) normalised by their values at infinite dilution in absence of any external field. The effective rotational decay is enhanced in the disordered state while it is similar to the equilibrium case in the low strain regime and a significant slowing down is observed in the high strain state. At small strain amplitudes the values are slightly smaller than unity as we expect from the analysis of the equilibrium behaviour with respect to volume fraction and elongation (cf. section 3.3) [154]. In the regularly structured twinned fcc regime (I) the diffusion is basically constant with increasing strain amplitude.

In the transition region $0.2 < \gamma_{\max} < 0.3$ we observe an elevated orientational diffusion where it is steeply curved with respect to the strain amplitude. On entering the high strain regime it jumps back to a value close to its initial value at rest. With increasing strain amplitude the orientational diffusion then slightly decreases. In the high strain regime we observe a state showing enhanced coupling of the dumbbells' orientations in space and time. For the higher aspect ratio (system B) we observe similar behaviour, while the peak in the disordered state (II) at about $\gamma_{\max} \approx 0.25$ is much less pronounced. Also, the normalised inverse time scales are slightly smaller than in the former system (A), which is an expected packing effect (cf. section 3.3) [154]. At the low aspect ratio of state point C, which does not show a fully disordered state, we observe essentially unhindered rotational relaxation and

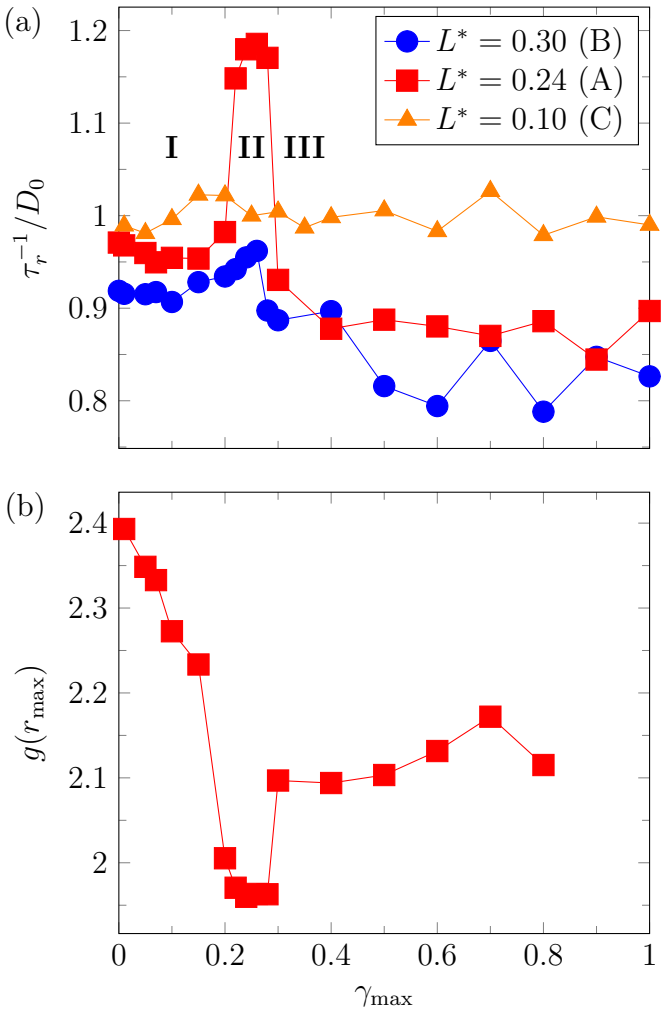

Figure 4.11: (a) Orientational relaxation constants from the decays of the C_1 correlation functions for state points A, B and C, and (b) contact values of the radial distribution function $g_s(r)$ on increasing strain amplitude for state point A. Adapted with permission from N. Heptner, F. Chu, Y. Lu, P. Lindner, M. Ballauff, and J. Dzubiella, Phys. Rev. E **92**, 052311 (2015) [122]. Copyright © 2015, American Physical Society.

virtually no influence of the shear amplitude.

The transition behaviour of the rotational diffusion corresponds well to the contact value analysis, allowing us to connect structure and kinetics. Figure 4.11b shows the values of the radial distribution function (RDF) $g_s(r)$ at contact ($r = r_{\max}$) of system A with $L^* = 0.24, \phi = 0.60$. On approaching the melting strain at about $\gamma_{\max} = 0.2$ the contact value $g_s(\sigma) = \Gamma_E/\Gamma_0$ rises slightly. At the transition from the ordered shear twinned system (I) to the disordered state (II) the contact value shows a distinct jump of about 10 %. A smaller jump is observed at the transition

to the ordered high strain regime where the contact value is less than in in the disordered state and reaches a plateau at about $g_s(r_{\max}) \approx 2.1$. Following the inverse relationship of diffusion and contact value in the Enskog approximation eq. (2.60), thus the diffusivity increases drastically in the transition region (II).

4.3 Summary and conclusions

The structures and the corresponding rheological response defines three distinct states in our investigation. In combination of the experimental data and our NEBD simulation results we show at the aspect ratios of $L^* = 0.24$ and $L^* = 0.3$, that the sequence of steady-state structures is qualitatively different from the hard sphere case. Furthermore, the NEBD study indicates that a novel partially oriented sliding-layer state is stable at high strain amplitudes. We have here provided evidence that the mild anisotropy of dumbbell-shaped particles leads to qualitative changes in the nature of the non-equilibrium phase transitions of plastic crystals of spherical colloids under oscillatory shear, in particular that the continuous transition observed in spherical systems transforms into a discontinuous one. The latter phenomenon must be attributed to rotational-translational couplings [73], absent in nearly spherical systems that apparently lead to dramatic changes in the structural and stress relaxation behaviour. In fact, we have shown in the prior chapter simulations that plastic crystals of dumbbells exhibit a dramatic increase of the linear shear response for high packing fractions above a critical aspect ratio of about 0.15 [154]. With respect to the sequence of shear-induced states, the type and the dynamics of the equilibrium to twinned crystal transition remains an interesting issue, which may stimulate a future study. These strong transitions have substantial implications for the rheological yielding behaviour of colloidal PCs. The experimental results also show a frequency and time dependency of the rheology, which we attribute to a dynamical slowing down. The present results also demonstrate that the thermosensitive dumbbell particles introduced before [62] serve as an excellent and versatile model system for mildly anisotropic colloids to study their equilibrium and non-equilibrium structural and phase behaviour.

Chapter 5

Summary and Outlook

In this work, we have been able to connect simulations in equilibrium and shear conditions to novel experiments on an anisotropic colloidal model system. We have systematically shown the effect of mildly anisotropic particles compared to the guinea pig of colloidal physics. The results on the equilibrium structure show expected correlations in the spatial dimension and we have observed packing effects gaining importance from an elongation about $L^* = 0.2$ in the diffusion coefficients. In fact, we have in our analysis of equilibrium Brownian dynamics (BD) simulations that plastic crystals (PCs) of dumbbells exhibit a dramatic increase of the linear shear response for high packing fractions above a critical aspect ratio of about 0.15.

In the non-equilibrium study, we have provided evidence that the weak anisotropy of dumbbell-shaped particles leads to qualitative changes in the nature of the non-equilibrium transitions compared to spherical colloids under oscillatory shear Strikingly, one finds that the continuous transition observed in spherical systems transforms into a discontinuous one when increasing the aspect ratio. Also we have systematically shown that the behaviour of the hard sphere system is retained for dumbbells at very small aspect ratios. When increasing the aspect ratio further, the transition turns out to be rather vigorous and mediated by a disordered state. The onset of the deviation from the hard-sphere behaviour in the sheared system is in accord with the findings from the equilibrium study. The experimental results additionally show a frequency and time dependency of the rheology, which we attribute to a dynamical slowing down. The present results also demonstrate that the thermosensitive dumbbell particles introduced before [62] serve as an excellent and versatile model system for mildly anisotropic colloids to study their equilibrium and nonequilibrium structural and phase behaviour. Remarkably, the particles exhibit a non-vanishing orientational correlation in the novel partially ordered sliding layer state at high strain amplitudes. The latter phenomenon must be attributed

to rotational-translational couplings [73], absent in nearly spherical systems that apparently lead to dramatic changes in the structural and stress relaxation behaviour. In combination with rheology and scattering data [62, 115, 119] this study indicates clearly that even relatively small anisotropies of the particles have a vigorous impact on the mechanical properties of colloids. Furthermore, this thesis clarifies, that the double yielding behaviour of hard dumbbells are of structural origin. In contrast, the known double yielding events in colloidal glasses have been linked to local dynamic phenomena such as Brownian and shear-induced cage-escape [112].

This study may trigger further investigation on the type and nature of the equilibrium to twinned face-centered cubic (fcc) transition. Here, the polycrystalline nature of typical crystals and the nucleation of layers under shear is out of scope in the present work but may be accessible to larger-scale simulations.

Revisiting the time scales that are introduced in the experiments by increasing the elongation remains an interesting issue, as they are not captured in the present simulations neglecting many-body hydrodynamics. Understanding this phenomenon may also be of great interest for the (colloidal) glass community.

Furthermore, switching crystals of low aspect ratio colloids by shear is still an intriguing idea. As a well-controlled experimental model system is now available, which we have proven to correspond very well to the known predictions of the phase diagram as well as our non-equilibrium investigation, other protocols may be employed. Also the Péclet numbers could be increased, though the latter option is most probably limited by the boundaries of the existence of the translationally ordered states.

From the theoretical point of view, it is worthwhile to develop a minimal model for a detailed insight into the coupling of rotation and translation of low aspect ratio colloids. This would help to further elucidate the underlying statistical mechanics of the problem.

With a more application-oriented focus, it could also be possible to investigate the photonic band structure of a sheared colloidal crystal. Further investigation in this direction could help clarify if mechanical perturbation can be used to manipulate the bands of reflected and travelling light in plastic crystals.

Appendix

A.1 Transient melting and nucleation of steady ordered non-equilibrium states

Depending on the initial configuration, we find transient melting of the initially crystalline structure before the high-strain layered structure nucleates. We observe this transient to last for a time window which depends on the frequency (number of oscillations). After tens of Brownian times the steady sliding layer state emerges from this melt.

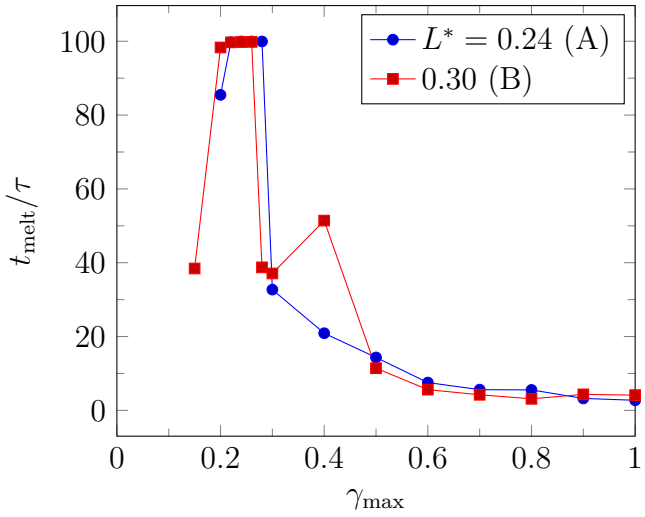

Figure A1: Time spent in a molten state characterised by a $Q_4 < 0.04$ threshold.

In fig. A1 the time spans t_{melt} spent in a transient melt are depicted. A value of $t_{\mathrm{melt}} = 100\tau$ relates to the system being molten for the entire simulation time. In the high shear regime, the time between melting of the initial structure and nucleation of the depends on the strain amplitude at a fixed frequency.

A.2 Single-particle diffusion coefficients

The single-particle diffusion coefficients calculated using the shell-bead model (SHM) model are presented in fig. A2.

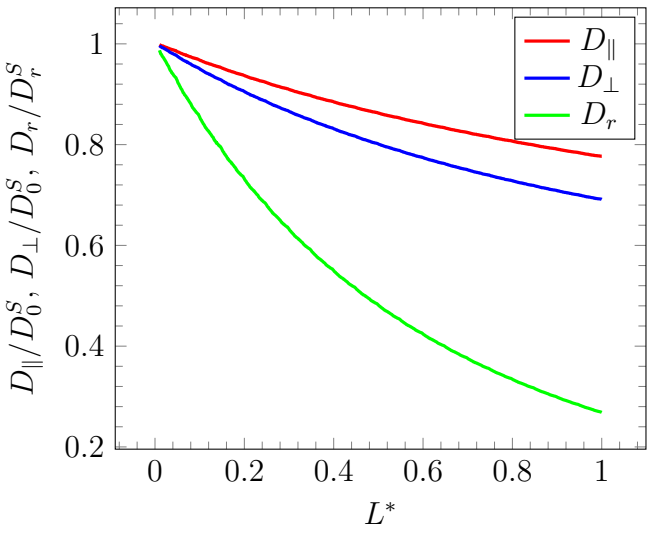

Figure A2: Normalised single-particle diffusion coefficients of dumbbells versus the elongation L^*.

A.3 Implementation of the Brownian dynamics method

In listing A1, the reader finds the key parts of the implementation of the BD method following eqs. (2.16), (2.17), (2.19) and (2.20). If shear is used, the coefficients associated with shear-affected terms have to be updated in every time step before updating the coordinates. It may be necessary to adjust the time step respecting the maximum shear rate.

Listing A1: Updating the BD coefficients and coordinates.

```
/*
 * set the method's coefficients
 */
template <typename T> inline void
   EulerExpl_RotShearFullTorque<T>::update_coeff(
   MyBox_LEy<T>& box, std::vector<T>& inp) {
  /*
   * constants
   */
```

```
  /* parallel */
  this->c(0)[0] = this->dt() * inp[0];
  this->c(0)[1] = std::sqrt(2. * this->c(0)[0]);
  this->c(0)[2] = this->dt() * box.peclet_gamma_.val(0);
  std::clog << "# c_par = " << this->c(0)[0] << " " <<
     this->c(0)[1] << " " << this->c(0)[2] << endl;

  /* perpendicular */
  this->c(1)[0] = this->dt() * inp[1];
  this->c(1)[1] = std::sqrt(2. * this->c(1)[0]);
  this->c(1)[2] = this->dt() * box.peclet_gamma_.val(0);
  std::clog << "# c_perp = " << this->c(1)[0] << " " <<
     this->c(1)[1] << " " << this->c(1)[2] << endl;

  /* rotational */
  this->c(2)[0] = this->dt() * inp[2];
  this->c(2)[1] = std::sqrt(2. * this->c(2)[0]);
  this->c(2)[2] = this->dt() * box.peclet_gamma_.val(0);
  std::clog << "# c_rot = " << this->c(2)[0] << " " <<
     this->c(2)[1] << " " << this->c(2)[2] << endl;
}

/*
 * update the method's coefficients if shear is used
 */
template <typename T> inline void
   EulerExpl_RotShearFullTorque<T>::update_coeff(
   MyBox_LEy<T>& box) {
    if (box.peclet_omega_.val(0) != .0)
      /*
       * $\dot{\gamma}(t) = \gamma_{\text{max}} * \omega
           * \cos(\omega t)
       */
      box.peclet_gamma_.val(0) = box.strain_amplitude_.
         val(0) * box.peclet_omega_.val(0) * std::cos(box
         .peclet_omega_.val(0) * this->time() );
```

```
\lstset{
  language=csh,
  breaklines=true,
  tabsize=2,
  basicstyle=\ttfamily
}
    /*
     * $v_x(t) = \Pe_\gamma(t) L_y$
     */
    box.v(0) = box.peclet_gamma_.val(0) * box.len(1);
    /*
     * periodic displacement $\delta x(t) = \sum_i v_x(
        t_i) dt
     */
    box.disp(0) += box.v(0) * this->dt();

    /*
     * update integrator coefficients
     */
    this->c(0)[2] = this->dt() * box.peclet_gamma_.val
       (0);
    this->c(1)[2] = this->dt() * box.peclet_gamma_.val
       (0);
    this->c(2)[2] = this->dt() * box.peclet_gamma_.val
       (0);
}

template <typename T> inline void
   EulerExpl_RotShearFullTorque<T>::update(Dumbbells_set<
   T>& set, Dumbbells_set<T>& set_new, Pair_Force<T, std
   ::vector<T> >& force, MyBox<T>& bbox, MyListVerlet
   const& vlist) {
  if (set.size() != this->rnd_.size() ) {
    this->rnd_.resize(set.size(), std::vector<T>(5, .0)
       );
```

```
}

/* generate random variates */
for (size_t i = 0; i < this->rnd_.size(); i ++) {
  for (size_t j = 0; j < this->rnd_[i].size(); j ++) {
    this->rnd_[i][j] = static_cast<T>(
       gsl_ran_ugaussian(this->rng_) );
  } /* j */
} /* i */

MyBox_LEy<T>& box = *static_cast<MyBox_LEy<T>* >(&bbox
   );

std::vector<T>& c_par = this->c_[0];
std::vector<T>& c_perp = this->c_[1];
std::vector<T>& c_rot = this->c_[2];

if (box.peclet_omega_.val(0) != .0 || box.
   peclet_gamma_.val(0) != 0.0) {
  this->update_coeff(box);
}

/* update separation vectors and squared distances*/
set.update_rsep(vlist);

/* update inter-bead forces */
set.update_fbead0(force, vlist);

/* compute total forces on particles from total forces
    on beads */
set.update_ftot();

/* update parallel and perpendicular force components
   */
set.update_fpar();
set.update_fperp();
```

```
/* update torques */
set.update_torque();

/* update parallel parts of the COM coordinates */
#pragma omp parallel for shared(set, set_new)

for (size_t i = 0; i < set.size(); i ++) {
  for (size_t p = 0; p < 3; p ++) {
    T frnd = this->rnd_[i][0];
    T displ_f = c_par[0] * set.fpar(i)[p];
    T displ_r = c_par[1] * frnd * set.dir(i)[p];
    set_new.com_par()[i][p] = set.com_par()[i][p] +
       displ_f + displ_r;
  } /* p */
} /* i */

/* update perpendicular coordinates */
#pragma omp parallel for shared(set, set_new)

for (size_t i = 0; i < set.size(); i ++) {
  for (size_t p = 0; p < 3; p ++) {
    T frnd1 = this->rnd_[i][1];
    T frnd2 = this->rnd_[i][2];
    T displ_f = c_perp[0] * set.fperp(i)[p];
    T displ_r = c_perp[1] * frnd1 * set.e1(i)[p] +
       c_perp[1] * frnd2 * set.e2(i)[p];
    set_new.com_perp()[i][p] = set.com_perp()[i][p] +
       displ_f + displ_r;
  } /* p */
} /* i */

/*
 * update COM as r = r_\par + r_\perp
 */
#pragma omp parallel for shared(set, set_new)
```

```
for (size_t i = 0; i < set.size(); i ++) {

  for (size_t p = 0; p < 3; p ++) {
    set_new.com()[i][p] = set_new.com_perp()[i][p] +
       set_new.com_par()[i][p];
  } /* p */

  /*
   * add flow contribution
   * $\Delta t \dot\gamma(t) y$
   */
  set_new.com()[i][0] += c_par[2] * (box.wrap(set.com
     ()[i][1], 1) - .5 * box.len(1) );

} /* i */

/* update directors */
#pragma omp parallel for shared(set, set_new)

for (size_t i = 0; i < set.size(); i ++) {
  T norm = .0;

  /*
   * angular displacement by particle interactions
   */
  std::vector<T> disp_ang = std::vector<T>(3, .0);

  /*
   * $\Delta \vec{u}^p = \vec{T}^p \times \vec{u}$
   */
  vecprod<T>(disp_ang, set.torque(i), set.dir(i) );

  for (size_t p = 0; p < 3; p ++) {
    T frnd1 = this->rnd_[i][3];
    T frnd2 = this->rnd_[i][4];
```

```
      T displ_f = c_rot[0] * disp_ang[p];
      T displ_r = c_rot[1] * frnd1 * set.e1(i)[p] +
         c_rot[1] * frnd2 * set.e2(i)[p];
      set_new.dir(i)[p] = set.dir(i)[p] + displ_f  +
         displ_r;
    } /* p */

    /* add flow contribution */
    set_new.dir(i)[0] += c_rot[2] * (std::pow(set.dir(i)
       [1], 3) + std::pow(set.dir(i)[2], 2) * set.dir(i)
       [1]);
    set_new.dir(i)[1] -= c_rot[2] * (set.dir(i)[0] * std
       ::pow(set.dir(i)[1], 2) );
    set_new.dir(i)[2] -= c_rot[2] * (set.dir(i)[0] * set
       .dir(i)[1] * set.dir(i)[2]);

    /* normalize director */
    norm = norm_2<T, std::vector<T> >(set_new.dir(i) );
    for (size_t p = 0; p < 3; p ++) {
      set_new.dir(i)[p] /= norm;
    } /* p */
  } /* i */
}
```

A.4 Implementation of the scattering function $I(\mathbf{q})$

The code for calculating the scattering function as defined in eqs. (2.33) and (2.34) is presented in listing A2. The function for calculating $I(\mathbf{q})$ expects before-selected scattering vectors. The numerical integration which is needed for $A(\mathbf{q};\mathbf{u})$ is the bottleneck of this calculation.

Listing A2: Calculating the scattering function with explicit Scattering amplitudes.

```
/*
 * \brief calculate scattering intensity I(q) including
    scattering amplitudes A_DB(q, u_i)
 */
```

```
template <typename T> inline void Dumbbells_set<T>::ioq(
   MyFunction<T>& s, MyFunction<T>& poq, size_t const&
   maxintervals) {
  this->update_com();
  this->update_dir();

  #pragma omp parallel for shared(s)

  for (size_t i = 0; i < s.size(); i ++) {
    std::vector<T>& q_ijk = s.x(i);
    T sum_cos = .0;
    T sum_sin = .0;
    T poq_sum_cos = .0;

    ScatterAmp adb_l = ScatterAmp(maxintervals);

    Dumbbell db_l = Dumbbell(this->lstar(0) );

    for (size_t p = 0; p < 3; p ++)
      db_l.q_[p] = q_ijk[p];

    for (size_t l = 0; l < this->N_; l ++){
      std::vector<T>& r = this->com()[l];

      for (size_t p = 0; p < 3; p ++)
        db_l.u_[p] = this->dir(l)[p];

      T a_l = adb_l.eval(db_l, integrand_dumbbell);

      /* $\vec{q} \cdot \vec{r}$ */
      T qdotr = sprod<T>(q_ijk, r);

      sum_cos += a_l * std::cos(qdotr);
      sum_sin += a_l * std::sin(qdotr);
      poq_sum_cos += a_l;
    } /* l */
```

```
    sum_cos = std::pow(sum_cos, 2);
    sum_sin = std::pow(sum_sin, 2);
    s[i] = (sum_cos + sum_sin) / this->N_;

    poq_sum_cos = std::pow(poq_sum_cos, 2);
    poq[i] = poq_sum_cos / this->N_;
  } /* i */

}

/*
 * \brief calculate integrand for given particle at
    specific $t$
 * \return value of the integrand $A(t; \vec{q}, \vec{u
    })$
 */
double Dumbbell::integrand(double const& t) const {
  std::vector<double> const& q = this->q_;
  std::vector<double> const& u = this->u_;

  double const qdotu = sprod<double>(q, u);
  double const qn = norm_2<double, std::vector<double>
     >(q);
  double const costheta = qdotu / qn;
  double const sintheta = std::sqrt(1. - std::pow(
     costheta, 2) );

  /* $w(t)$ */
  double const w = std::cos(0.5 * qdotu * (t + this->
     lstar_) );
  /* $s(t)$ */
  double const s = 0.5 * qn * sintheta * std::sqrt(1. -
     std::pow(t, 2) );
```

```
  return 0.25 * M_PI * std::pow(this->sigma_, 3) * (1. -
      std::pow(t, 2) ) * w * (gsl_sf_bessel_J0(s) +
     gsl_sf_bessel_Jn(2, s) );
}

double ScatterAmp::eval(Dumbbell& particle, double
   integrand(double , void* ) ){
  gsl_function f;
  f.function = integrand;
  f.params = static_cast<void*>(&particle);

  /* gsl integration options */
  int scheme = 1;
  double error;
  double const epsrel = 1e-5;
  double const epsabs = 1e-6;
  /* integral limits */
  double const a = particle.lower_bound();
  double const b = particle.upper_bound();

  /* prevent terminating the program on errors in gsl
     functions */
  gsl_set_error_handler_off();

  /* adaptive integration */
  int status = gsl_integration_qag(&f, a, b, epsabs,
     epsrel, this->maxintervals_, scheme, this->
     workspace_, &this->result_, &error);

  if (status) {
    std::cerr << particle.u_[0] << "␣" << particle.u_[1]
        << "␣" << particle.u_[2] << "␣" << particle.q_[0]
        << "␣" << particle.q_[1] << "␣" << particle.q_[2]
        << "␣" << this->eval() << std::endl;
  }
```

```
  return this->eval();
}
```

The scattering function can be projected to the interesting planes with the following scripts in listings A3 and A4:

Listing A3: Shell script for projection of $I(\mathbf{q})$

```
#! /usr/bin/env csh

set fname=$1
set dname="`basename␣$fname␣.dat`"

set oname=${dname}"_qy0.dat"
set fname0=${oname}

echo ${oname}
awk '($2 == .0){print}' $1 > ${oname}

set oname=${dname}"_xz.dat"

echo ${oname}
soq_prj_xz.awk ${fname} | sort -gs -k2,2 | sort -gs -k1
   ,1 | awk 'BEGIN{ko=0}{kn = $1; if (ko != kn && NR > 1)
    {print ""}; ko = kn; print}' > ${oname}

set oname=${dname}"_xz_qy0.dat"

echo ${fname0}

echo ${oname}
soq_prj_xz.awk ${fname0} | sort -gs -k2,2 | sort -gs -k1
   ,1 | awk 'BEGIN{ko=0}{kn = $1; if (ko != kn && NR > 1)
    {print ""}; ko = kn; print}' > ${oname}
```

Here the projection at $q_y = 0$ is implemented in Awk.

Listing A4: soq_prj_xz.awk

```
#! /usr/bin/awk -f
```

```
BEGIN {
}
{
  if (NF == 4 && !($1 + 0. != $1) ) {
    soq[$1, $3] += $4
    kx[$1, $3] = $1
    kz[$1, $3] = $3
    count[$1,$3] += 1.
  }
}
END{
  for (kk in soq) {
    print kx[kk], kz[kk], soq[kk]
  }
}
```

Bibliography

[1]A. Einstein, "Über die von der molekularkinetischen Theorie der Wärme geforderte Bewegung von in ruhenden Flüssigkeiten suspendierten Teilchen", Annalen der Physik **322**, 549–560 (1905).

[2]M. von Smoluchowski, "Zur kinetischen Theorie der Brownschen Molekularbewegung und der Suspensionen", Annalen der Physik **326**, 756–780 (1906).

[3]J. Perrin, "Mouvement Brownien et réalité moléculaire", Annales de chimie et de physique **18**, 5–114 (1909).

[4]C. G. de Kruif, T. Huppertz, V. S. Urban, and A. V. Petukhov, "Casein micelles and their internal structure", Adv. Colloid Interface Sci. **171–172**, 36–52 (2012).

[5]J.-G. Park, J. D. Forster, and E. R. Dufresne, "High-yield synthesis of monodisperse dumbbell-shaped polymer nanoparticles", J. Am. Chem. Soc. **132**, 5960–5961 (2010).

[6]A. van Blaaderen, "Materials science: colloids get complex", Nature **439**, 545–546 (2006).

[7]J. F. Galisteo-López, M. Ibisate, R. Sapienza, L. S. Froufe-Pérez, Á. Blanco, and C. López, "Self-assembled photonic structures", Adv. Mater. **23**, 30–69 (2010).

[8]S. C. Glotzer, and M. J. Solomon, "Anisotropy of building blocks and their assembly into complex structures", Nat. Mater. **6**, 557–562 (2007).

[9]J. K. Oh, R. Drumright, D. J. Siegwart, and K. Matyjaszewski, "The development of microgels/nanogels for drug delivery applications", Prog. Polym. Sci. **33**, 448–477 (2008).

[10]H. Longuet-Higgins, and B. Widom, "A rigid sphere model for the melting of argon", Mol. Phys. **8**, 549–556 (1964).

[11]D. J. Kraft, J. Groenewold, and W. K. Kegel, "Colloidal molecules with well-controlled bond angles", Soft Matter **5**, 3823–3826 (2009).

[12]D. M. Herlach, I. Klassen, P. Wette, and D. Holland-Moritz, "Colloids as model systems for metals and alloys: a case study of crystallization", J. Phys.: Condens. Matter **22**, 153101 (2010).

[13]V. J. Anderson, and H. N. W. Lekkerkerker, "Insights into phase transition kinetics from colloid science", Nature **416**, 811–815 (2002).

[14]E. Bianchi, R. Blaak, and C. N. Likos, "Patchy colloids: state of the art and perspectives", Phys. Chem. Chem. Phys. **13**, 6397 (2011).

[15]C. N. Likos, "Soft matter with soft particles", Soft Matter **2**, 478 (2006).

[16]A. Nikoubashman, G. Kahl, and C. N. Likos, "Flow quantization and nonequilibrium nucleation of soft crystals", Soft Matter **8**, 4121–4131 (2012).

[17]M. Ballauff, and Y. Lu, ""Smart"nanoparticles: preparation, characterization and applications", Polymer **48**, 1815–1823 (2007).

[18]Y. Lu, and M. Ballauff, "Thermosensitive core–shell microgels: from colloidal model systems to nanoreactors", Prog. Polym. Sci. **36**, 767–792 (2011).

[19]A. Stein, and R. C. Schroden, "Colloidal crystal templating of three-dimensionally ordered macroporous solids: materials for photonics and beyond", Curr. Opin. Solid State Mater. Sci. **5**, 553–564 (2001).

[20]N. Osterman, I. Poberaj, J. Dobnikar, D. Frenkel, P. Ziherl, and D. Babić, "Field-induced self-assembly of suspended colloidal membranes", Phys. Rev. Lett. **103**, 228301 (2009).

[21]I. D. Hosein, S. H. Lee, and C. M. Liddell, "Dimer-based three-dimensional photonic crystals", Adv. Funct. Mater. **20**, 3085–3091 (2010).

[22]J. D. Forster, J. G. Park, M. Mittal, H. Noh, C. F. Schreck, C. S. O'Hern, H. Cao, E. M. Furst, and E. R. Dufresne, "Assembly of optical-scale dumbbells into dense photonic crystals", ACS Nano **5**, 6695–6700 (2011).

[23]K. P. Velikov, T. van Dillen, A. Polman, and A. van Blaaderen, "Photonic crystals of shape-anisotropic colloidal particles", Appl. Phys. Lett. **81**, 838–840 (2002).

[24]K. P. Velikov, A. Moroz, and A. van Blaaderen, "Photonic crystals of core-shell colloidal particles", Appl. Phys. Lett. **80**, 49–51 (2002).

[25]C. Liddell, and C. Summers, "Monodispersed ZnS dimers, trimers, and tetramers for lower symmetry photonic crystal lattices", Adv. Mater. **15**, 1715–1719 (2003).

[26]P. N. Pusey, W. C. K. Poon, S. M. Ilett, and P. Bartlett, "Phase behaviour and structure of colloidal suspensions", J. Phys.: Condens. Matter **6**, A29–A36 (1994).

[27]P. N. Pusey, and W. van Megen, "Phase behaviour of concentrated suspensions of nearly hard colloidal spheres", Nature **320**, 340–342 (1986).

[28]Y. L. Wu, D. Derks, A. van Blaaderen, and A. Imhof, "Melting and crystallization of colloidal hard-sphere suspensions under shear", Proc. Natl. Acad. Sci. U.S.A. **106**, 10564–10569 (2009).

[29]C. P. Royall, J. Dzubiella, M. Schmidt, and A. van Blaaderen, "Nonequilibrium sedimentation of colloids on the particle scale", Phys. Rev. Lett. **98** (2007).

[30]C. P. Royall, W. C. K. Poon, and E. R. Weeks, "In search of colloidal hard spheres", Soft Matter **9**, 17–27 (2013).

[31]P. N. Pusey, E. Zaccarelli, C. Valeriani, E. Sanz, W. C. K. Poon, and M. E. Cates, "Hard spheres: crystallization and glass formation", Phil. Trans. R. Soc. A **367**, 4993–5011 (2009).

[32]W. C. K. Poon, E. R. Weeks, and C. P. Royall, "On measuring colloidal volume fractions", Soft Matter **8**, 21–30 (2012).

[33]P. N. Pusey, W. van Megen, P. Bartlett, B. J. Ackerson, J. G. Rarity, and S. M. Underwood, "Structure of crystals of hard colloidal spheres", Phys. Rev. Lett. **63**, 2753–2756 (1989).

[34]C. Radin, "Random close packing of granular matter", J Stat Phys **131**, 567–573 (2008).

[35]P. N. Pusey, and W. van Megen, "Observation of a glass transition in suspensions of spherical colloidal particles", Phys. Rev. Lett. **59**, 2083–2086 (1987).

[36]S. Torquato, T. M. Truskett, and P. G. Debenedetti, "Is random close packing of spheres well defined?", Phys. Rev. Lett. **84**, 2064–2067 (2000).

[37]B. Cipra, "Music of the spheres", Science **251**, 1028–1028 (1991).

[38]H. C. Andersen, J. D. Weeks, and D. Chandler, "Relationship between the hard-sphere fluid and fluids with realistic repulsive forces", Phys. Rev. A **4**, 1597–1607 (1971).

[39]F. Perrin, "Mouvement brownien d'un ellipsoide II. rotation libre et dépolarisation des fluorescences. translation et diffusion de molécules ellipsoidales", J. Phys. Radium **7**, 1–11 (1936).

[40]L. Onsager, "The effects of shape on the interaction of colloidal particles", Ann. N.Y. Acad. Sci. **51**, 627–659 (1949).

[41]F. Perrin, "Mouvement brownien d'un ellipsoide I. dispersion diélectrique pour des molécules ellipsoidales", J. Phys. Radium **5**, 497–511 (1934).

[42]H. Löwen, "Brownian dynamics of hard spherocylinders", Phys. Rev. E **50**, 1232–1242 (1994).

[43]J. Schwarz-Linek, C. Valeriani, A. Cacciuto, M. E. Cates, D. Marenduzzo, A. N. Morozov, and W. C. K. Poon, "Phase separation and rotor self-assembly in active particle suspensions", Proc. Natl. Acad. Sci. U.S.A. **109**, 4052–4057 (2012).

[44]D. Frenkel, B. M. Mulder, and J. P. McTague, "Phase diagram of a system of hard ellipsoids", Phys. Rev. Lett. **52**, 287–290 (1984).

[45]C. Vega, and P. A. Monson, "Plastic crystal phases of hard dumbbells and hard spherocylinders", J. Chem. Phys. **107**, 2696–2697 (1997).

[46]J. Talbot, D. Kivelson, M. P. Allen, G. T. Evans, and D. Frenkel, "Structure of the hard ellipsoid fluid", J. Chem. Phys. **92**, 3048–3057 (1990).

[47]P. Bolhuis, and D. Frenkel, "Tracing the phase boundaries of hard spherocylinders", J. Chem. Phys. **106**, 666–687 (1997).

[48]A. Kuijk, D. V. Byelov, A. V. Petukhov, A. van Blaaderen, and A. Imhof, "Phase behavior of colloidal silica rods", Faraday Discuss. **159**, 181–199 (2012).

[49]R. Blaak, D. Frenkel, and B. M. Mulder, "Do cylinders exhibit a cubatic phase?", J. Chem. Phys. **110**, 11652 (1999).

[50]B. Liu, T. H. Besseling, M. Hermes, A. F. Demirörs, A. Imhof, and A. van Blaaderen, "Switching plastic crystals of colloidal rods with electric fields", Nat. Commun. **5**, 3092 (2014).

[51]R. Zhang, and K. S. Schweizer, "Theory of coupled translational-rotational glassy dynamics in dense fluids of uniaxial particles", Phys. Rev. E **80**, 011502 (2009).

[52]P. M. Johnson, C. M. van Kats, and A. van Blaaderen, "Synthesis of colloidal silica dumbbells", Langmuir **21**, 11510–11517 (2005).

[53]E. B. Mock, and C. F. Zukoski, "Investigating microstructure of concentrated suspensions of anisotropic particles under shear by small angle neutron scattering", J. Rheol. **51**, 541–559 (2007).

[54]E. B. Mock, and C. F. Zukoski, "Determination of static microstructure of dilute and concentrated suspensions of anisotropic particles by ultra-small-angle x-ray scattering", Langmuir **23**, 8760–8771 (2007).

[55]E. B. Mock, H. De Bruyn, B. S. Hawkett, R. G. Gilbert, and C. F. Zukoski, "Synthesis of anisotropic nanoparticles by seeded emulsion polymerization", Langmuir **22**, 4037–4043 (2006).

[56]R. C. Kramb, R. Zhang, K. S. Schweizer, and C. F. Zukoski, "Glass formation and shear elasticity in dense suspensions of repulsive anisotropic particles", Phys. Rev. Lett. **105**, 055702 (2010).

[57]R. C. Kramb, and C. F. Zukoski, "Exploration of the volume fraction above which suspensions of spherical and weakly anisotropic colloid particles cannot flow", J. Rheol. **55**, 1085–1101 (2011).

[58]R. C. Kramb, and C. F. Zukoski, "Nonlinear rheology and yielding in dense suspensions of hard anisotropic colloids", J. Rheol. **55**, 1069–1084 (2011).

[59]M. Hoffmann, Y. Lu, M. Schrinner, M. Ballauff, and L. Harnau, "Dumbbell-shaped polyelectrolyte brushes studied by depolarized dynamic light scattering", J. Phys. Chem. B **112**, 14843–14850 (2008).

[60]D. Nagao, C. M. van Kats, K. Hayasaka, M. Sugimoto, M. Konno, A. Imhof, and A. van Blaaderen, "Synthesis of hollow asymmetrical silica dumbbells with a movable inner core", Langmuir **26**, 5208–5212 (2010).

[61]B. Peng, H. R. Vutukuri, A. van Blaaderen, and A. Imhof, "Synthesis of fluorescent monodisperse non-spherical dumbbell-like model colloids", J. Mater. Chem. **22**, 21893–21900 (2012).

[62]F. Chu, M. Siebenbürger, F. Polzer, C. Stolze, J. Kaiser, M. Hoffmann, N. Heptner, J. Dzubiella, M. Drechsler, Y. Lu, and M. Ballauff, "Synthesis and characterization of monodisperse thermosensitive dumbbell-shaped microgels.", Macromol. Rapid Commun. **33**, 1042–1048 (2012).

[63]M. Hoffmann, C. S. Wagner, L. Harnau, and A. Wittemann, "3D Brownian diffusion of submicron-sized particle clusters", ACS Nano **3**, 3326–3334 (2009).

[64]M. Hoffmann, M. Siebenbürger, L. Harnau, M. Hund, C. Hanske, Y. Lu, C. S. Wagner, M. Drechsler, and M. Ballauff, "Thermoresponsive colloidal molecules", Soft Matter **6**, 1125–1128 (2010).

[65]D. A. Weitz, and M. Oliveria, "Fractal structures formed by kinetic aggregation of aqueous gold colloids", Phys. Rev. Lett. **52**, 1433–1436 (1984).

[66]K. A. Dawson, G. Foffi, F. Sciortino, P. Tartaglia, and E. Zaccarelli, "Mode-coupling theory of colloids with short-range attractions", J. Phys.: Condens. Matter **13**, 9113–9126 (2001).

[67]K. A. Dawson, "The glass paradigm for colloidal glasses, gels, and other arrested states driven by attractive interactions", Curr. Opin. Colloid Interface Sci. **7**, 218–227 (2002).

[68]S. Auer, and D. Frenkel, "Suppression of crystal nucleation in polydisperse colloids due to increase of the surface free energy", Nature **413**, 711–713 (2001).

[69]D. A. Kofke, and P. G. Bolhuis, "Freezing of polydisperse hard spheres", Phys. Rev. E **59**, 618–622 (1999).

[70]E. Sanz, C. Valeriani, E. Zaccarelli, W. C. K. Poon, P. N. Pusey, and M. E. Cates, "Crystallization mechanism of hard sphere glasses", Phys. Rev. Lett. **106**, 215701 (2011).

[71]M. Siebenbürger, M. Fuchs, H. H. Winter, and M. Ballauff, "Viscoelasticity and shear flow of concentrated, noncrystallizing colloidal suspensions: comparison with mode-coupling theory", J. Rheol. **53**, 707–726 (2009).

[72]M. Siebenbürger, M. Ballauff, and T. Voigtmann, "Creep in colloidal glasses", Phys. Rev. Lett. **108**, 255701 (2012).

[73]R. M. Lynden-Bell, and K. H. Michel, "Translation-rotation coupling, phase transitions, and elastic phenomena in orientationally disordered crystals", Rev. Mod. Phys. **66**, 721–762 (1994).

[74]S. J. Singer, and R. Mumaugh, "Monte carlo study of fluid–plastic crystal coexistence in hard dumbbells", J. Chem. Phys. **93**, 1278–1286 (1990).

[75]C. Vega, E. P. A. Paras, and P. A. Monson, "On the stability of the plastic crystal phase of hard dumbbell solids", J. Chem. Phys. **97**, 8543–8548 (1992).

[76]C. Vega, E. P. A. Paras, and P. A. Monson, "Solid–fluid equilibria for hard dumbbells via monte carlo simulation", J. Chem. Phys. **96**, 9060–9072 (1992).

[77]M. Marechal, and M. Dijkstra, "Stability of orientationally disordered crystal structures of colloidal hard dumbbells", Phys. Rev. E **77**, 061405 (2008).

[78]R. Ni, and M. Dijkstra, "Crystal nucleation of colloidal hard dumbbells", J. Chem. Phys. **134**, 034501 (2011).

[79]E. P. A. Paras, C. Vega, and P. A. Monson, "Application of cell theory to the thermodynamic properties of hard dumbbell solids", Mol. Phys. **77**, 803–821 (1992).

[80]K. W. Wojciechowski, "Monte Carlo simulations of highly anisotropic two-dimensional hard dumbbell-shaped molecules: nonperiodic phase between fluid and dense solid", Phys. Rev. B **46**, 26–39 (1992).

[81]K. W. Wojciechowski, D. Frenkel, and A. C. Bra ńka, "Nonperiodic solid phase in a two-dimensional hard-dimer system", Phys. Rev. Lett. **66**, 3168–3171 (1991).

[82]A. van Blaaderen, "Colloids under external control", MRS Bull. **29**, 85–90 (2004).

[83]D. Nagao, M. Sugimoto, A. Okada, H. Ishii, M. Konno, A. Imhof, and A. van Blaaderen, "Directed orientation of asymmetric composite dumbbells by electric field induced assembly", Langmuir **28**, 6546–6550 (2012).

[84]S. E. Paulin, and B. J. Ackerson, "Observation of a phase transition in the sedimentation velocity of hard spheres", Phys. Rev. Lett. **64**, 2663–2666 (1990).

[85]A. F. Demirörs, P. M. Johnson, C. M. van Kats, A. van Blaaderen, and A. Imhof, "Directed self-assembly of colloidal dumbbells with an electric field", Langmuir **26**, 14466–14471 (2010).

[86]A. van Blaaderen, M. Dijkstra, R. van Roij, A. Imhof, M. Kamp, B. W. Kwaadgras, T. Vissers, and B. Liu, "Manipulating the self assembly of colloids in electric fields", Eur. Phys. J. Spec. Top. **222**, 2895–2909 (2013).

[87]M. Marechal, M. Dijkstra, M. Marechal and M. Dijkstra, "Colloidal hard dumbbells under gravity: structure and crystallization", Soft Matter **7**, 1397–1408 (2011).

[88]H. Schmidle, S. Jäger, C. K. Hall, O. D. Velev, and S. H. L. Klapp, "Two-dimensional colloidal networks induced by a uni-axial external field", Soft Matter **9**, 2518–2524 (2013).

[89]H. Löwen, "Colloidal soft matter under external control", J. Phys.: Condens. Matter **13**, R415–R432 (2001).

[90]M. C. Wendl, "General solution for the couette flow profile", Phys. Rev. E **60**, 6192–6194 (1999).

[91]N. Koumakis, A. B. Schofield, and G. Petekidis, "Effects of shear induced crystallization on the rheology and ageing of hard sphere glasses", Soft Matter **4**, 2008–2018 (2008).

[92]M. D. Haw, W. C. K. Poon, P. N. Pusey, P. Hebraud, and F. Lequeux, "Colloidal glasses under shear strain", Phys. Rev. E **58**, 4673–4682 (1998).

[93]A. Zaccone, D. Gentili, H. Wu, M. Morbidelli, and E. Del Gado, "Shear-driven solidification of dilute colloidal suspensions", Phys. Rev. Lett. **106**, 138301 (2011).

[94]B. Ackerson, "Shear-induced partial translational ordering of a colloidal solid", Phys. Rev. A **30**, 906–918 (1984).

[95]B. Ackerson, "Shear induced order of hard-sphere suspensions", J. Phys.: Condens. Matter **2**, SA389–SA392 (1990).

[96]B. Ackerson, and N. Clark, "Sheared colloidal suspensions", Physica A **118**, 221–249 (1983).

[97]B. Ackerson, "Shear induced order in equilibrium colloidal liquids", Physica A **174**, 15–30 (1991).

[98]B. J. Ackerson, and N. A. Clark, "Shear-induced melting", Phys. Rev. Lett. **46**, 123–126 (1981).

[99]S. Paulin, B. Ackerson, and M. Wolfe, "Equilibrium and shear induced nonequilibrium phase behavior of PMMA microgel spheres", J. Colloid. Interf. Sci. **178**, 251–262 (1996).

[100]B. J. Ackerson, and P. N. Pusey, "Shear-induced order in suspensions of hard-spheres", Phys. Rev. Lett. **61**, 1033–1036 (1988).

[101]M. D. Haw, W. C. K. Poon, and P. N. Pusey, "Direct observation of oscillatory-shear-induced order in colloidal suspensions", Phys. Rev. E **57**, 6859–6864 (1998).

[102]T. H. Besseling, M. Hermes, A. Fortini, M. Dijkstra, A. Imhof, and A. van Blaaderen, "Oscillatory shear-induced 3D crystalline order in colloidal hard-sphere fluids", Soft Matter **8**, 6931–6939 (2012).

[103]W. Loose, and B. J. Ackerson, "Model-calculations for the analysis of scattering data from layered structures", J. Chem. Phys. **101**, 7211–7220 (1994).

[104]C. Dux, and H. Versmold, "Light diffraction from shear ordered colloidal dispersions", Phys. Rev. Lett. **78**, 1811–1814 (1997).

[105]Y. Yan, J. Dhont, C. Smits, and H. Lekkerkerker, "Oscillatory-shear-induced order in nonaqueous dispersions of charged colloidal spheres", Physica A **202**, 68–80 (1994).

[106]R. Blaak, S. Auer, D. Frenkel, and H. Löwen, "Crystal nucleation of colloidal suspensions under shear", Phys. Rev. Lett. **93**, 068303 (2004).

[107]L. B. Chen, M. K. Chow, B. J. Ackerson, and C. F. Zukoski, "Rheological and microstructural transitions in colloidal crystals", Langmuir **10**, 2817–2829 (1994).

[108]L. B. Chen, B. J. Ackerson, and C. F. Zukoski, "Rheological consequences of microstructural transitions in colloidal crystals", J. Rheol. **38**, 193–216 (1994).

[109]R. Biehl, and T. Palberg, "Modes of motion in a confined colloidal suspension under shear", Europhys. Lett. **66**, 291–295 (2004).

[110]T. Palberg, and R. Biehl, "Sheared colloidal crystals in confined geometry: a real space study on stationary structures under shear", Faraday Discuss. **123**, 133–143 (2002).

[111]B. J. Ackerson, "Shear induced order and shear processing of model hard-sphere suspensions", J. Rheol. **34**, 553–590 (1990).

[112]N. Koumakis, J. F. Brady, and G. Petekidis, "Complex oscillatory yielding of model hard-sphere glasses", Phys. Rev. Lett. **110**, 178301 (2013).

[113]N. Koumakis, and G. Petekidis, "Two step yielding in attractive colloids: transition from gels to attractive glasses", Soft Matter **7**, 2456–2470 (2011).

[114]N. Koumakis, M. Laurati, S. U. Egelhaaf, J. F. Brady, and G. Petekidis, "Yielding of hard-sphere glasses during start-up shear", Phys. Rev. Lett. **108**, 098303 (2012).

[115]F. Chu, N. Heptner, Y. Lu, M. Siebenbürger, P. Lindner, J. Dzubiella, and M. Ballauff, "Colloidal plastic crystals in a shear field", Langmuir **31**, 5992–6000 (2015).

[116]R. C. Kramb, and C. F. Zukoski, "Yielding in dense suspensions: cage, bond, and rotational confinements", J. Phys.: Condens. Matter **23**, 035102 (2011).

[117]R. Zhang, and K. S. Schweizer, "Dynamic free energies, cage escape trajectories, and glassy relaxation in dense fluids of uniaxial hard particles", J. Chem. Phys. **133**, 104902 (2010).

[118]R. Zhang, and K. S. Schweizer, "Theory of nonlinear elasticity, stress-induced relaxation, and dynamic yielding in dense fluids of hard nonspherical colloids", J. Chem. Phys. **136**, 154902 (2012).

[119]F. Chu, "Dumbbell-shaped colloids - equilibrium and nonequilibrium phase behaviour", PhD thesis (2014).

[120]R. L. Mills, D. H. Liebenberg, and J. C. Bronson, "Melting properties and ultrasonic velocity of nitrogen to 20 kbar", J. Chem. Phys. **63**, 4026–4031 (1975).

[121]R. L. Mills, B. Olinger, and D. T. Cromer, "Structures and phase diagrams of N_2 and CO to 13 gpa by x-ray diffraction", J. Chem. Phys. **84**, 2837–2845 (1986).

[122]N. Heptner, F. Chu, Y. Lu, P. Lindner, M. Ballauff, and J. Dzubiella, "Nonequilibrium structure of colloidal dumbbells under oscillatory shear", Phys. Rev. E **92**, 052311 (2015).

[123]J. Hansen, and I. McDonald, *Theory of simple liquids*, 3rd (Academic Press, 2006).

[124]J. Rotne, and S. Prager, "Variational treatment of hydrodynamic interaction in polymers", J. Chem. Phys. **50**, 4831 (1969).

[125]L. D. Favro, "Theory of the rotational brownian motion of a free rigid body", Phys. Rev. **119**, 53–62 (1960).

[126]M. Doi, and S. F. Edwards, *The theory of polymer dynamics*, International Series of Monographs on Physics (Oxford University Press, 1988).

[127]J. G. de la Torre, and B. Carrasco, "Hydrodynamic properties of rigid macromolecules composed of ellipsoidal and cylindrical subunits", Biopolymers **63**, 163–167 (2002).

[128]H. Brenner, "Coupling between the translational and rotational brownian motions of rigid particles of arbitrary shape II. general theory", J. Colloid Interface Sci. **23**, 407–436 (1967).

[129]A. L. Kholodenko, and J. F. Douglas, "Generalized Stokes-Einstein equation for spherical particle suspensions", Phys. Rev. E **51**, 1081–1090 (1995).

[130]W. B. Russel, D. A. Saville, and W. R. Schowalter, *Colloidal dispersions*, Cambridge monographs on mechanics and applied mathematics (Cambridge University Press, 1992).

[131]D. M. Heyes, and A. C. Brańka, "The influence of potential softness on the transport coefficients of simple fluids", J. Chem. Phys. **122**, 234504 (2005).

[132]J. A. Barker, and D. Henderson, "Perturbation theory and equation of state for fluids. ii. a successful theory of liquids", J. Chem. Phys. **47**, 4714–4721 (1967).

[133]D. M. Heyes, and P. J. Mitchell, "Linear viscoelasticity of concentrated hard-sphere dispersions", J. Phys.: Condens. Matter **6**, 6423–6436 (1994).

[134]T. N. Phung, J. F. Brady, and G. Bossis, "Stokesian dynamics simulation of brownian suspensions", J. Fluid Mech. **313**, 181 (1996).

[135]D. L. Ermak, "Computer-simulation of charged particles in solution. I. technique and equilibrium properties", J. Chem. Phys. **62**, 4189–4196 (1975).

[136]A. W. Lees, and S. F. Edwards, "Computer study of transport processes under extreme conditions", J. Phys. C: Solid State Phys. **5**, 1921–1929 (1972).

[137]M. Allen, and D. J. Tildesley, *Computer simulation of liquids* (Clarendon Press, 1989).

[138]B. Carrasco, and J. G. de la Torre, "Hydrodynamic properties of rigid particles: comparison of different modeling and computational procedures", Biophys. J. **76**, 3044–3057 (1999).

[139]J. G. de la Torre, G. D. Echenique, and A. Ortega, "Improved calculation of rotational diffusion and intrinsic viscosity of bead models for macromolecules and nanoparticles", J. Phys. Chem. B **111**, 955–961 (2007).

[140]F. G. Diaz, J. G. de la Torre, and J. J. Freire, "Hydrodynamic interaction effects in the rheological properties of hookean dumbbells in steady shear-flow - a brownian dynamics simulation study", Polymer **30**, 259–264 (1989).

[141]M. M. Tirado, C. L. Martinez, and J. G. de la Torre, "Comparison of theories for the translational and rotational diffusion-coefficients of rod-like macromolecules - application to short DNA fragments", J. Chem. Phys. **81**, 2047–2052 (1984).

[142]T. Kirchhoff, H. Löwen, and R. Klein, "Dynamical correlations in suspensions of charged rodlike macromolecules", Phys. Rev. E **53**, 5011–5022 (1996).

[143]J. Schneider, W. Hess, and R. Klein, "A dumbbell model for the structure of charged, rodlike macromolecules in dilute-solution", Macromolecules **19**, 1729–1732 (1986).

[144]H. Kaya, "Scattering from cylinders with globular end-caps", J. Appl. Crystallogr. **37**, 223–230 (2004).

[145]P. J. Steinhardt, D. R. Nelson, and M. Ronchetti, "Bond-orientational order in liquids and glasses", Phys. Rev. B **28**, 784–805 (1983).

[146]R. Kubo, "Statistical-mechanical theory of irreversible processes. I. general theory and simple applications to magnetic and conduction problems", J. Phys. Soc. Jpn. **12**, 570–586 (1957).

[147]M. S. Green, "Markoff random processes and the statistical mechanics of time-dependent phenomena. II. irreversible processes in fluids", J. Chem. Phys. **22**, 398–413 (1954).

[148]B. Felderhof, and R. Jones, "Linear response theory of the viscosity of suspensions of spherical brownian particles", Physica A **146**, 417–432 (1987).

[149]T. A. J. Lenstra, Z. Dogic, and J. K. G. Dhont, "Shear-induced displacement of isotropic-nematic spinodals", J. Chem. Phys. **114**, 10151 (2001).

[150]B. J. Berne, and R. Pecora, *Dynamic light scattering* (Dover, 2000).

[151]J. K. G. Dhont, *An introduction to dynamics of colloids* (Elsevier Science, 1996).

[152]J. Mewis, and N. J. Wagner, *Colloidal suspension rheology* (Cambridge University Press, 2012).

[153]K. Hyun, M. Wilhelm, C. O. Klein, K. S. Cho, J. G. Nam, K. H. Ahn, S. J. Lee, R. H. Ewoldt, and G. H. McKinley, "A review of nonlinear oscillatory shear tests: analysis and application of large amplitude oscillatory shear (LAOS)", Prog. Polym. Sci. **36**, 1697–1753 (2011).

[154]N. Heptner, and J. Dzubiella, "Equilibrium structure and fluctuations of suspensions of colloidal dumbbells", Mol. Phys. **113**, 2523–2530 (2015).

List of Acronyms

ACF autocorrelation function. 30

BD Brownian dynamics. iii, v, 9, 10, 13, 18, 19, 23, 27, 29, 31, 61, 64

COM centre of mass. iii, 19, 20, 23–28, 37, 40, 41, 51

CP close packed. 7

DACF directional autocorrelation function. 29, 42, 43

DDLS depolarised dynamic light scattering. 30

DLS dynamic light scattering. 30

F fluid. 7, 37–39, 41–43

fcc face-centered cubic. viii, 9, 23, 27, 50, 52–56, 58, 62, 93

hcp hexagonal close packed. 9, 27, 50, 57, 93

HS hard sphere. 44, 45, 48

LHS left-hand side. 16

MC Monte Carlo. 6, 31

MSD mean square displacement. 28

NEBD non-equilibrium Brownian dynamics. iii, v, 47–49, 53, 55, 60, 94

PBC periodic boundary conditions. 22, 23

PC plastic crystal. iii, v, 5–7, 10–12, 31, 37–39, 41–44, 47, 60, 61

PCF pair correlation function. 37

RDF radial distribution function. 24, 29, 30, 37, 59

RHS right-hand side. 16

SACF stress autocorrelation function. 29, 43–45

SANS small-angle neutron scattering. iii, 12, 13, 31, 33, 47–49, 55, 93, 94

SHM shell-bead model. 22, 23, 64

VACF velocity autocorrelation function. 28, 40, 41

List of Symbols

D_0 single-particle centre-of-mass diffusion.

D_0^S free single sphere diffusion.

$D_\parallel$ single-particle diffusion coefficient parallel to the long axis.

$D_\perp$ single-particle diffusion coefficient perpendicular to the long axis.

D_r single-particle rotational diffusion coefficient.

D_r^L orientational long-time diffusion.

D_r^S free single sphere diffusion.

D_s^L long-time diffusion.

L centre-to-centre distance of a dumbbell.

L^* particle elongation.

L_α simulation box length $\alpha = x, y, z$.

N particle number.

P_2^α orientational order measure.

Q_4 averaged local bond order parameter.

T Temperature.

W_4 averaged local bond order parameter.

$\gamma_{\max}$ strain amplitude.

κ interaction steepness parameter.

$\langle \dots \rangle$ time average.

$\langle \dots \rangle_{\text{cycle}}$ strain cycle average.

Pe Péclet number.

Pe_r rotational Péclet number.

ϕ volume fraction.

ρ particle number density.

ρ^N N-particle density distribution.

σ interaction length.

$\sigma_{\alpha\beta}$ stress tensor entry.

τ Brownian time.

τ_r orientational relaxation constant in the non-equilibrium steady state.

d sphere diameter.

$g(r)$ centre-of-mass radial distribution function.

$g_s(r)$ site-site radial distribution function.

$g_{P_2}(r)$ orientational pair correlation function.

k_B Boltzmann constant.

List of Figures

Schlusserklärung

Hiermit erkläre ich, dass ich die vorliegende Arbeit selbstständig verfasst und keine anderen als die hier angegebenen Quellen und Hilfsmitteln benutzt habe.

Weiterhin erkläre ich, dass ich nicht anderweitig mit oder ohne Erfolg versucht habe, eine Dissertation einzureichen oder mich einer Doktorprüfung zu unterziehen.

Berlin, den 20. Mai 2016

Danksagung

Ich möchte mich bei meinem Betreuer Prof. Dr. Joachim Dzubiella bedanken. Neben der Möglichkeit in diesem spannenden Feld zu arbeiten, hat seine ständige Beratung und Orientierung in meiner Forschung großen Anteil gehabt.

Ganz besonderer Dank gilt Dr. Fangfang Chu, deren großartige Systeme und Experimente essentiell in unserer Kollaboration waren, die Prof. Dr. Matthias Ballauff mitinitiiert und mit großem Engagement und Weitsicht vorangetrieben hat.

Ich bedanke mich bei Prof. Dr. Holger Stark und Prof. Dr. Benjamin Lindner dafür, dass sie sich bereit erklärt haben, meine Arbeit zu begutachten. Außerdem danke ich Prof. Dr. Matthias Ballauff und Prof. Dr. Stefan Kowarik für Ihre Bereitschaft der Prüfungskommission anzugehören.

Großer Dank gebührt Karol Palczynski, Matt Barrett, Cemil Yigit, Annegret Günther und Gregor Weiß für das Lesen und Kritisieren dieser Arbeit.